ANNUAL REVIEWS

Polarization and Vorticity in the Quark–Gluon Plasma

Francesco Becattini[1] and Michael A. Lisa[2]

[1]Dipartimento di Fisica e Astronomia, Università degli Studi di Firenze, Florence I-50019, Italy; email: becattini@fi.infn.it

[2]Department of Physics, The Ohio State University, Columbus, Ohio 43210, USA; email: lisa.1@osu.edu

ANNUAL REVIEWS CONNECT

www.annualreviews.org

- Download figures
- Navigate cited references
- Keyword search
- Explore related articles
- Share via email or social media

Keywords

polarization, quark–gluon plasma, magnetic field, heavy-ion collisions, hydrodynamics, vorticity

Abstract

The quark–gluon plasma (QGP) produced by collisions between ultrarelativistic heavy nuclei is well described in the language of hydrodynamics. Noncentral collisions are characterized by very large angular momentum, which in a fluid system manifests as flow vorticity. This rotational structure can lead to a spin polarization of the hadrons that eventually emerge from the plasma, and thus these collisions provide experimental access to flow substructure at unprecedented detail. Recently, the first observations of Λ hyperon polarization along the direction of collisional angular momentum were reported. These measurements are in broad agreement with hydrodynamic and transport-based calculations and reveal that the QGP is the most vortical fluid ever observed. However, there remain important tensions between theory and observation that might be fundamental in nature. In the relatively mature field of heavy-ion physics, the discovery of global hyperon polarization and 3D simulations of the collision have opened an entirely new direction of research. We discuss the current status of this rapidly developing area and directions for future research.

Contents

1. INTRODUCTION

Collisions between heavy nuclei at ultrarelativistic energies create a quark–gluon plasma (QGP) (1–5) that is characterized by colored partons as dynamic degrees of freedom. Since the mid-1980s, a large community has systematically studied these collisions to extract insights about quantum chromodynamics (QCD) matter under extreme conditions. The resulting field of relativistic heavy-ion physics is by now relatively mature. With the early realization that the QGP in these collisions is a nearly perfect fluid, hydrodynamics has been the dominant theoretical framework in which to study the system.

Much of the evidence for the fluid nature of the QGP has been based on the response of the bulk medium to azimuthal (to the beam direction) anisotropies in the initial energy density (6). Measured azimuthal correlations are well reproduced by modulations in the outward-directed flow fields in the hydro simulations. However, although heavy-ion collisions involve huge angular momentum densities (10^3–$10^4\,\hbar$ over volumes of about 250 fm^3), relatively less focus has been placed on the consequences of this angular momentum.

In any fluid, angular momentum manifests as vorticity in the flow field. In the QGP, the coupling between rotational motion and quantum spin can lead to polarization of hadrons emitted from fluid cells, driven by the local vorticity of the cell. In 2017, the first experimental observation of vorticity-driven polarization in heavy ions was reported (7). This development has generated intense theoretical activity and further experimental study. In this article, we review the tremendous progress and current understanding of the vortical nature of the QGP. This line of investigation,

which has only just begun, represents one of the few truly new directions in the soft sector of relativistic heavy-ion physics in many years.

In the next section, we place these studies in a larger context of similar phenomena in other physical systems and define geometrical conventions required for the heavy-ion case. In Section 3, we then discuss theoretical tools employed to model the complex rotational dynamics of the plasma and its manifestation in particle polarization. In Section 4, we discuss experimental measurements and observational systematics (we note broad agreement between observation and theory but tension in some important aspects). We conclude our review with open questions and an outlook.

2. QUARK–GLUON PLASMA, HYDRODYNAMICS, AND VORTICITY

Evidence collected over a time span of more than 10 years suggests that the QGP produced in collisions of nuclei at relativistic energies is transiently (i.e., for about 10^{-22} s) a nearly perfect fluid. After an initial preequilibrium stage, the strongly interacting system produced in the collisions of the two nuclei quickly achieves local thermodynamic equilibrium (with a typical interaction length much smaller than the scale of variation of densities) and, hence, reaches a plasma state. Thereafter, the plasma expands and cools, remaining close to local equilibrium; this part of the process can be effectively described by relativistic hydrodynamic equations. Around the pseudocritical QCD temperature of 160 MeV (8, 9), it breaks up into hadrons (10) and ceases to be a fluid. After a short kinetic stage of interacting hadron gas, the strongly stable particles stop colliding (freeze out) and freely travel toward the detectors. The cornerstone of this model is the observation that momentum spectra of produced hadrons are very well reproduced by the assumption of a local Bose–Einstein or Fermi–Dirac distribution function (for vanishing chemical potentials):

$$f(x, p) = \frac{1}{\exp[\beta \cdot p] \pm 1},$$

1.

where $\beta = (1/T)u(x)$ is the four-temperature vector including temperature and the four-velocity hydrodynamic field $u(x)$. Equation 1 applies to the local fluid cell and should be integrated thereafter over the freeze-out 3D hypersurface (see **Figure 2**), which is defined as the boundary of local thermodynamic equilibrium, giving rise to what is known in the field as the Cooper–Frye formula (11). Indeed, the freeze-out hypersurface is analogous to the last scattering surface in the cosmological expansion on which the background electromagnetic radiation froze out.

As mentioned above, local thermodynamic equilibrium is achieved—and a plasma at finite temperature is formed—at quite an early time in the process (see **Figure 2**). This hypothesis is confirmed by the success of the hydrodynamic equations in determining the flow field $u(x)$ in Equation 1. In particular, the model is able to successfully account for the observed anisotropies of the momentum spectra in the transverse plane perpendicular to the beam line (refer to **Figure 1**) as a function of the azimuthal angle. These anisotropies—encoded in the Fourier coefficients v_n—suggest that the viscosity of the QGP must be very small compared with the entropy density, with a ratio close to the conjectured universal lower bound of $\hbar/4\pi$ (13). The smallness of the viscosity/entropy ratio implies a very short interaction length, of the same order of magnitude as the thermal wavelength of the elementary constituents: quarks and gluons. The kinetic description—whose prerequisite is a mean free path much longer than particle wavelength—is therefore dubious. The QGP is a system that cannot be described in terms of colliding particles or quasi-particles; rather, it is a system of strongly interacting fields in local thermodynamic equilibrium (strongly interacting QGP) and is, hence, still hydrodynamic.
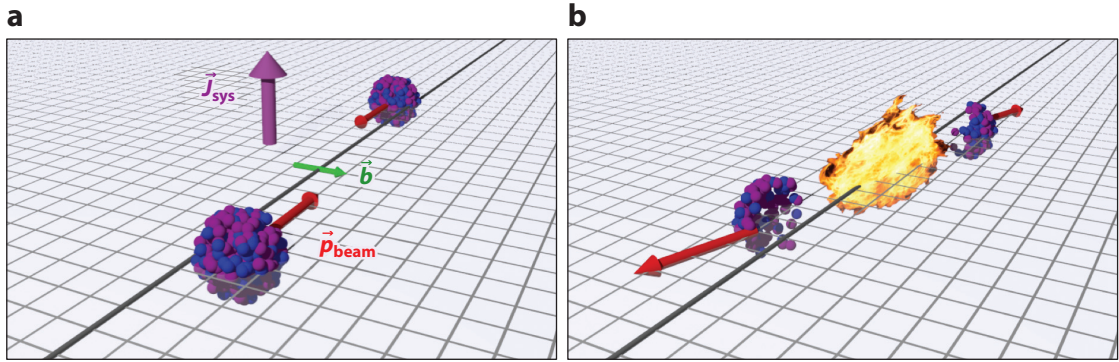
Figure 1

A heavy-ion collision at relativistic energy in the center-of-mass frame. (*a*) The relevant geometrical and physical quantities characterizing a collision are shown. (*b*) The quark–gluon plasma is formed out of the colliding nucleons of the nuclear overlapping region. The spectator deflection in panel *b* is exaggerated for clarity.

Recently, the exploration of the QGP made a significant advance. The measurement of polarization of emitted hadrons has made it clear that a new probe is accessible, which may provide a wealth of new and complementary information. In particular, in the hydrodynamic paradigm, while the momentum spectra provide direct information about the velocity and the temperature field, polarization is linked to the vorticity and more generally to the gradients of these fields (see Section 3). In ideal hydrodynamics, particle distribution functions, such as Equation 1, are determined by intensive thermodynamic quantities of the local cell in the local rest frame, such as temperature and chemical potentials related to the various charges (e.g., baryon number, electric charge). Likewise, assuming that spin degrees of freedom locally equilibrate, vorticity potentially determines the spin–charge distribution of particles—that is, the number of spin-up versus
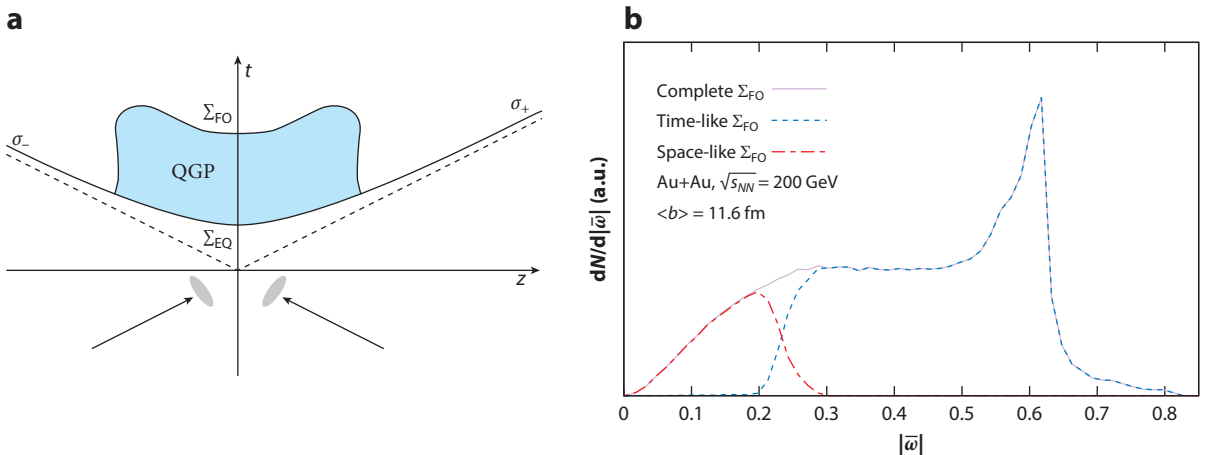
Figure 2

(*a*) Space-time diagram of a collision of two nuclei. In the hydrodynamic model, local equilibrium is believed to occur on the hyperbola Σ_{EQ} (the initial 3D hypersurface of the thermalized QGP) and to cease at the 3D hypersurface Σ_{FO}. (*b*) Distribution of the amplitude of thermal vorticity $|\varpi| = \sqrt{|\varpi_{\mu\nu}\varpi^{\mu\nu}|}$ at the freeze-out hypersurface Σ_{FO}, calculated with the ECHO-QGP code under the same conditions as in Reference 12 with a freeze-out temperature of 130 MeV. The red dashed line indicates the contribution of the space-like part, whereas the blue dashed line indicates that of the time-like part. Abbreviation: QGP, quark–gluon plasma.

spin-down particles (see Section 3). Vorticity should be then considered a further intensive thermodynamic quantity that is necessary for description of the local fluid. In a sense, vorticity is an extra substructure of a hydrodynamic cell. This property makes polarization a very sensitive probe of the dynamical process leading to the QGP formation and its evolution. As mentioned in Section 1, this field has only just begun, and polarization may lead to a number of developments that have not yet been envisioned.

2.1. Vorticity and Polarization: Overview

While the QGP formed in heavy-ion collisions is only a few times larger than a nucleus, heavy ions are used to form a bulk system that is significantly larger than the confinement volume characteristic of a hadron. In other words, the system that is formed is much larger than the typical microscopic interaction scale, and such a separation of scales (the hydrodynamic limit) makes it possible to talk about a fluid and to use hydrodynamics as an effective tool to describe its evolution; in the hydro language, the Knudsen number is sufficiently small (14). Under such circumstances, the variation of the flow field in space and time can be slow enough to be dealt with as the macroscopic motion of bulk matter and vorticity as well. As will become clear in Section 3, the vortical structure is probed by the spin of hadrons that freeze out from local fluid cells in a state of local thermodynamic equilibrium, as discussed above. More specifically, the presence of a vortical motion (as well as an acceleration and a temperature gradient) entails a modification of Equation 1 such that the distribution function becomes nontrivially dependent on the spin degrees of freedom.

That spin and vorticity are tightly related is not a new insight, and yet there are relatively few examples of physical systems that show the effect of the coupling between mechanical angular momentum of bulk matter and the quantum spin of particles that compose (or emerge from) that matter. Two seminal measurements were reported nearly simultaneously more than a century ago. Barnett (15) observed that an initially unmagnetized steel cylinder generates a magnetic field upon being rotated. In the same year, Einstein & de Haas (16) observed the complementary effect: A stationary unmagnetized ferromagnetic object will begin to rotate upon introduction of an external magnetic field. In both cases, the phenomenon is rooted in the conservation of total angular momentum on the one hand and in equipartition of angular momentum—that is, thermodynamic equilibrium—on the other. In the Barnett effect, the angular momentum that is imparted through a forced rotation gets partly distributed to the quantum spin of the constituents, and once thermodynamic equilibrium is reached, a stable magnetic field is generated as a consequence of the polarization of matter. In the Einstein–de Haas effect, the external magnetic field implies, at thermodynamic equilibrium, a polarization of matter, and hence an angular momentum; if the magnetic field does not provide torque, the body should start spinning to conserve the initial vanishing angular momentum. Indeed, a quantitative understanding of these phenomena was possible only a decade later with the discovery of the electron spin and anomalous gyromagnetic ratio.

Another example is found in low-energy heavy-ion reactions in which a beam with a kinetic energy of $E_{kin} \approx 30$ MeV per nucleon is incident on a stationary target. (In high-energy physics terms, $\sqrt{s_{NN}} - 2m_p \approx 15$ MeV, where m_p is the proton mass.) This scenario reflects the regime of quasi-compound-nucleus formation, in which the short-lived system is assumed to rotate as a whole to first order. At high beam energies ($E_{kin} \gtrsim 50$ AMeV), projectile fragments are expected to experience positive deflection (see Section 2.2) due to collisional and bulk compression during the collision. At lower energies, collisions are Pauli-suppressed, and attractive nuclear surface interactions are expected to produce an orbiting motion that leads to negative deflection. Disentangling the interplay between these physical mechanisms requires determination of $\hat{J}_{sys}$, which has been achieved (17, 18) by correlating the circular polarization of γ-rays with forward fragment

deflection angles. These measurements represent the first observation of global polarization in (nonrelativistic) heavy-ion reactions.

In the above cases, the bulk mechanical motion is basically rigid-body rotation.[1] Only recently (19) has mechanically induced spin polarization been observed in a fluid. Liquid Hg flowing through a channel experiences viscous forces along the channel walls, which generate a local vorticity field whose strength and direction vary as a function of position. Hydrodynamic vorticity–spin coupling then produces a corresponding electron polarization field, which Saitoh et al. (20) measured using the inverse spin Hall effect. That experiment, in which both the vorticity and the induced polarization were observable, was important in establishing the phenomenon of spin polarization in fluids.

Regarding all the cases listed above, polarization in relativistic heavy ions possesses two unique features. First, its measurement is not mediated by a magnetic field (like in the Barnett effect); rather, the mean spin of particles is directly observed, which is not possible in ordinary matter. Second, and maybe more importantly, the system at hand—QGP at very high energy—is almost neutral by charge conjugation (i.e., C-even). If it was precisely neutral, the observation of polarization by magnetization would be impossible because particles and antiparticles have opposite magnetic moments. In fact, Λ and $\bar{\Lambda}$ in relativistic nuclear collisions at high energy have almost the same mean spin, which is an unmistakable signature of thermomechanically driven polarization. If the electromagnetic field (or any other C-odd mean field) was responsible for this effect, the sign of the mean spin vector components would be opposite. Hence, while for nonrelativistic matter (without antimatter) it is impossible to resolve polarization by rotation and by magnetization— which lie at the very heart of the Barnett and Einstein–de Haas effects—in relativistic matter, because of the existence of antiparticles, the rotation and magnetization effects can be distinguished, and QGP is the first relativistic system through which the distinction has been observed.

2.2. Geometry of a Nuclear Collision

Figure 1*a* sketches the geometry of a heavy-ion collision in its center-of-mass frame before contact. One nucleus is designated as the beam and the other as the target,[2] and the impact parameter **b** points from the center of the target to the center of the beam, perpendicular to the beam momentum $\mathbf{p}_{\mathrm{beam}}$. The vectors **b** and $\mathbf{p}_{\mathrm{beam}}$ span the reaction plane indicated by the grid. The total angular momentum of the collision can be expressed as $\mathbf{J}_{\mathrm{sys}} = \mathbf{b} \times \mathbf{p}_{\mathrm{beam}}$.

Figure 1*b* sketches the situation after the collision. In the participant–spectator model (21) commonly used at high energies, a fireball at midrapidity is produced by the sudden and violent deposition of energy when participant nucleons overlap and collide. Meanwhile, projectile nucleons that do not overlap with oncoming nucleons in the target are considered spectators and continue with their forward motion essentially unchanged, to undergo nuclear fragmentation later.

However, in reality this distinction is not so sharp: The forward spectators do receive a sideways repulsive impulse during the collision, as indicated in **Figure 1***b* by the deflected momentum arrows. The case shown in the figure is deflection to positive angles, which enables us to distinguish the case at much lower energy (e.g., 18), at which attractive forces can produce negative deflection. In the parlance of relativistic collisions (22), the positive deflection corresponds to positive directed flow (v_1) in the forward direction ($v_1 > 0$ when $y \approx y_{\mathrm{beam}}$).

---

[1]Low-energy compound nuclei have surface vibrations and breathing but generally do not feature internal fluid flow structure.

[2]This initial designation is of course arbitrary, but the convention must be kept consistent. In the age of collider-mode nuclear physics, confusion is not uncommon and can lead to sign errors.

This deflection is important. While we are especially interested in the vortical structure of the fireball at midrapidity, we need to know the direction of the angular momentum, which must by symmetry give the average direction of vorticity. Forward detectors at large pseudorapidity are used to estimate $\hat{\mathbf{J}}_{\text{sys}}$ on an event-by-event basis, as discussed below.

Regarding coordinate systems and conventions, we note that it is common to define a coordinate system in which $\hat{\mathbf{z}} \equiv \hat{\mathbf{p}}_{\text{beam}}$ and $\hat{\mathbf{x}} \equiv \hat{\mathbf{b}}$. In this case, $\hat{\mathbf{J}} = -\hat{\mathbf{y}}$; the azimuthal angle of $\hat{\mathbf{b}}$ about $\hat{\mathbf{p}}_{\text{beam}}$ in some coordinate system (say, the floor of the experimental facility) is often referred to as the reaction plane angle Ψ_{RP}. The aforementioned forward detectors use spectator fragment deflection to determine the event plane angle $\Psi_{\text{EP},1}$. Standard techniques have been developed (22) to determine the event plane and the resolution with which it approximates Ψ_{RP}—that is, the direction $\hat{\mathbf{b}}$.

Because the size and angular momentum of the QGP fireball depend on the overlap between the colliding nuclei, an estimate of the impact parameter's magnitude is also important. Standard estimators (23), typically based on the charged particle multiplicity measured at midrapidity, quantify the centrality of each collision in terms of fraction of inelastic cross section. Head-on ($|\mathbf{b}| = \mathbf{0}$) and barely glancing collisions are said to have a centrality of 0% and 100%, respectively.

3. POLARIZATION IN RELATIVISTIC HEAVY-ION COLLISIONS: THEORY

The main theoretical challenge is to calculate the amount of polarization of observable particles once the initial condition of the collision is known—that is, the energy and the impact parameter of the two nuclei. The final outcome depends on the model of the collision (see Section 2) and on how the initial angular momentum may induce a global polarization of the particles.

The first calculation regarding global polarization in relativistic heavy-ion collisions was presented in Reference 24 based on a perturbative QCD–inspired model in which colliding partons are polarized by means of spin–orbit coupling. The amount of predicted polarization of Λ baryons was originally large (around 30%) and corrected thereafter by the same authors (25) to be less than 4%. Besides the apparent large uncertainty, the main problem of the collisional approach—at the quark–gluon level—is the difficulty of reconciling it with the evidence of a strongly interacting QGP, as pointed out in Section 2. Another problem lies in transferring the polarization at the quark–gluon level to final hadrons—a process that requires a detailed hadronization model and further assumptions. This scenario, however, has been further developed and is addressed in this section.

About the time when the first measurement of global Λ polarization at RHIC appeared (26), setting an upper limit of few percent, the idea of a polarization related to hydrodynamic motion, and in particular vorticity, was put forward (27, 28). If the QGP achieves and maintains local thermodynamic equilibrium until it decouples into freely streaming noninteracting hadrons, and if this model—as discussed in Sections 1 and 2—is very successful in describing the momentum spectra of particles, then there is no apparent reason why it should not be applicable to the spin degrees of freedom as well. Hence, polarization must be derivable from the fact that the system is in local thermodynamic equilibrium, whether in the plasma phase or in the hadron phase just before freeze-out. This idea establishes a link between spin and vorticity (more precisely, thermal vorticity, as described below) and makes it possible to obtain quantitative predictions at the hadronic level without needing a mechanism to transfer polarization from partons to hadrons. The actual quantitative relation for a relativistic fluid was first worked out in global equilibrium (29) and then in local equilibrium for spin $\frac{1}{2}$ particles (30).

For a particle with spin $\frac{1}{2}$, the mean spin vector is all that is needed to describe polarization (this is not the case for spin greater than $\frac{1}{2}$), and the relativistic formula was found to be, at leading order (30),

$$S^\mu(p) = -\frac{1}{8m}\epsilon^{\mu\rho\sigma\tau}p_\tau\frac{\int \mathrm{d}\Sigma_\lambda\, p^\lambda n_F(1-n_F)\varpi_{\rho\sigma}}{\int \mathrm{d}\Sigma_\lambda\, p^\lambda n_F}, \qquad \qquad 2.$$

where p is the four-momentum of the particle, and $n_F = (1 + \exp[\beta\cdot p - \mu Q/T])^{-1}$ is the Fermi–Dirac distribution with four-temperature β as in Equation 1 and with chemical potential μ coupled to a generic charge Q. The integration should be carried out over the freeze-out hypersurface (see **Figure 2**); in a sense, in the heavy-ion jargon this can be called the Cooper–Frye formula for the spin. The key ingredient in Equation 2 is the so-called thermal vorticity tensor $\varpi(x)$:

$$\varpi_{\mu\nu} = -\frac{1}{2}(\partial_\mu\beta_\nu - \partial_\nu\beta_\mu), \qquad \qquad 3.$$

that is, the antisymmetric derivative of the four-temperature vector. This quantity is adimensional in natural units, and it is the proper extension of the angular velocity/temperature ratio mentioned in Section 1. Hence, the spin depends at leading order on the gradients of the temperature–velocity fields—unlike momentum spectra, which at leading order depend on the temperature–velocity field itself. Thereby, polarization can provide complementary information about the hydrodynamic flow with respect to the spectra and their anisotropies. Equation 2 applies to antiparticles as well: In a charge-neutral fluid, the spin vector is expected to be the same for particles and antiparticles, which is a remarkable feature as emphasized in Section 2.1. Of note, Equation 2 implies that a particle within a fluid in motion at some space-time point x gets polarized according to (natural constants have been purposely restored):

$$\mathbf{S}^*(x,p) \propto \frac{\hbar}{KT^2}\gamma\mathbf{v}\times\nabla T + \frac{\hbar}{KT}\gamma(\boldsymbol{\omega}-(\boldsymbol{\omega}\cdot\mathbf{v})\mathbf{v}/c^2) + \frac{\hbar}{KT}\gamma\mathbf{A}\times\mathbf{v}/c^2, \qquad \qquad 4.$$

where $\gamma = 1/\sqrt{1-v^2/c^2}$, T is the temperature, and all three-vectors, including vorticity ($\boldsymbol{\omega}$), acceleration ($\mathbf{A}$), and velocity ($\mathbf{v}$), are observed in the particle rest frame. The decomposition in Equation 4 elucidates the thermodynamic forces responsible for polarization. The last term corresponds to the acceleration-driven polarization; its expression is reminiscent of the Thomas precession, and it is indeed tightly related to it (particle moving in an accelerated flow). The second term is the relativistic expression of polarization by vorticity. The first term is a polarization by combination of temperature gradient and hydrodynamic flow and is, to the best of our knowledge, a newly found effect.

The first hydrodynamic calculations based on Equation 2 predicted a global polarization of Λ baryons of a few percent at $\sqrt{s_{NN}} = 200$ GeV (31)—a prediction that was compatible with the previous experimental limit. The new measurements with larger statistics (see Section 4) then confirmed that the polarization value is of such an order of magnitude. Equation 2 then became a benchmark for most phenomenological calculations of polarization in heavy-ion collisions. In the subsections below, we review in some detail the status of the theoretical understanding of polarization in relativistic fluids and in nuclear collisions in particular.

3.1. Polarization in Statistical Mechanics

The calculation of spin at global or local thermodynamic equilibrium requires a quantum framework because spin is inherently a quantum observable. The most appropriate framework is thus

quantum statistical mechanics in a relativistic setting (since we are dealing with a relativistic fluid). However, many quantitative features can be found out starting from the simplest nonrelativistic case.

As a simple illustrative case, consider a rotating ideal gas with angular velocity $\boldsymbol{\omega}$ within a cylindrical vessel of radius R. At equilibrium, the statistical operator[3] reads (32)

$$\widehat{\rho} = \frac{1}{Z} \exp\left[-\frac{\widehat{H}}{T} + \frac{\boldsymbol{\omega} \cdot \widehat{\mathbf{J}}}{T}\right]. \qquad 5.$$

Because the particles are free, both the Hamiltonian and angular momentum operator are the sum of individual single-particle operators, and the density operator can be factorized. Because the total angular momentum includes both the orbital and spin part—that is, $\widehat{\mathbf{J}}_i = \widehat{\mathbf{L}}_i + \widehat{\mathbf{S}}_i$ for each particle i—the spin density matrix for a particle with momentum p turns out to be

$$\Theta(p)_{rs} \equiv \langle p, s | \widehat{\rho}_i | p, r \rangle = \frac{\langle p, s | \exp[\boldsymbol{\omega} \cdot \widehat{\mathbf{S}}_i / T] | p, r \rangle}{\sum_{t=-S}^{S} \langle p, t | \exp[\boldsymbol{\omega} \cdot \widehat{\mathbf{S}}_i / T] | p, t \rangle} = \delta_{rs} \frac{\exp[-s\omega/T]}{\sum_{t=-S}^{S} \exp[-t\omega/T]}, \qquad 6.$$

implying a mean spin vector of particles

$$\mathbf{S} = \widehat{\boldsymbol{\omega}} \frac{\partial}{\partial(\omega/T)} \frac{\sinh[(S + 1/2)\omega/T]}{\sinh[\omega/2T]} \simeq \frac{S(S+1)}{3} \frac{\boldsymbol{\omega}}{T}, \qquad 7.$$

where the last expression is leading order for small ratios ω/T. Equation 6 also implies that the so-called alignment Θ_{00} for spin 1 particles is quadratic in ω/T at leading order, which severely limits its observability in relativistic heavy-ion collisions (see also Section 5.3).

In the more general, relativistic case, the equilibrium operator in Equation 5 is replaced by (33)

$$\widehat{\rho} = \frac{1}{Z} \exp\left[-b_\mu \widehat{P}^\mu + \frac{1}{2}\varpi_{\mu\nu}\widehat{J}^{\mu\nu}\right], \qquad 8.$$

where b is a constant time-like four-vector and ϖ is the thermal vorticity, which, at global thermodynamic equilibrium, ought to be constant; $\widehat{P}$ and $\widehat{J}$ are the four-momentum and angular momentum–boost operators, respectively. Thermal vorticity includes both vorticity and acceleration besides the gradient of the temperature. For instance, at global equilibrium (34),

$$\varpi_{\mu\nu} = \epsilon_{\mu\nu\rho\sigma} \frac{1}{T} \omega^\rho u^\sigma + \frac{1}{T}(A_\mu u_\nu - A_\nu u_\mu), \qquad 9.$$

where u is the four-velocity, A is the four-acceleration, and ω is the vorticity four-vector. The entanglement of vorticity and acceleration is a typical signature of relativity, much like that of electric and magnetic fields in the electromagnetic tensor $F_{\mu\nu}$.

An intermediate step toward Equation 2 is the free single-particle quantum relativistic calculation. In this case, for a single particle, the operator from Equation 8 leads to the spin density matrix (35):

$$\Theta(p) = \frac{D^S([p]^{-1} \exp[(1/2)\varpi \; : \; \Sigma_S][p]) + D^S([p]^\dagger \exp[(1/2)\varpi \; : \; \Sigma_S^\dagger][p]^{-1\dagger})}{\mathrm{tr}(\exp[(1/2)\varpi \; : \; \Sigma_S] + \exp[(1/2)\varpi \; : \; \Sigma_S^\dagger])}, \qquad 10.$$

---

[3]Throughout this review, unit vectors are denoted with a small upper hat, and quantum operators are denoted with a wide upper hat.

where $D^S()$ stands for the $(2S + 1)$-dimensional representation of the group SL(2,C) universal covering of the Lorentz group, Σ_S are the $(2S + 1) \times (2S + 1)$ matrices representing the Lorentz generators, and $[p]$ is the so-called standard Lorentz transformation, which turns the unit time vector $\hat{\mathbf{t}}$ into the direction of the four-momentum p (36). The spin density matrix in Equation 10 implies a mean spin four-vector for sufficiently low values of the thermal vorticity:

$$S^\mu(p) = -\frac{1}{2m}\frac{S(S+1)}{3}\epsilon^{\mu\alpha\beta\nu}\varpi_{\alpha\beta}p_\nu,$$

11.

which is a direct relativistic extension of Equation 7 (37).

For a system of many particles, just like those emerging from nuclear collisions, one would take Equation 11 and average it over the different particle-emitting spots—that is, over the hydrodynamic cells of the freeze-out hypersurface. The result is Equation 2 but without the factor $(1 - n_F)$. This factor is the typical signature of Fermi statistics, and it naturally comes out in a quantum-field theoretical calculation. Indeed, this approach is taken in the original calculation at local thermodynamic equilibrium in Reference 30, where the density operator is the extension of Equation 8:

$$\widehat{\rho} = \frac{1}{Z}\exp\left[-\int_{\Sigma_{\mathrm{FO}}} \mathrm{d}\Sigma \; n_\mu(\widehat{T}^{\mu\nu}(x)\beta_\nu(x) - \zeta(x)\widehat{j}^\mu(x))\right],$$

12.

where $\beta_\nu(x)$ is the four-temperature function (dependent on space and time), $\zeta(x)$ is the ratio between chemical potential and temperature, and $\widehat{T}$ and $\widehat{j}$ are the stress–energy tensor and current operators, respectively. The integration should be done over the freeze-out 3D hypersurface (see **Figure 2**), which represents the boundary of local thermodynamic equilibrium. Indeed, calculating the mean spin vector from the density operator in Equation 12 is not straightforward, and some key assumptions are needed to get to Equation 2. The most important such assumption is the usual hydrodynamic limit: Microscopic lengths should be much smaller than the hydrodynamic scale—that is, $\beta(x)$ should be a slowly varying function. The second main assumption used in the original calculation (30) is an ansatz for the covariant Wigner function at global equilibrium with acceleration and rotation—that is, with the density operator in Equation 8. Despite these assumptions, there are good reasons to believe that the exact formula at leading order in thermal vorticity in a quantum field theory calculation would be Equation 2. Indeed, the same formula was found with a different approach based on the $\hbar$ expansion of the Wigner equation (38); furthermore, it is the only possible linear expression in ϖ that yields the correct single-particle expression in Equation 11 and the nonrelativistic limit. For instance, a term proportional to $\varpi^{\mu\nu}p_\nu$, even if orthogonal to p, would not yield correct limiting cases. What is still unknown is the global equilibrium exact formula at all orders in thermal vorticity including quantum statistics.

While the local equilibrium calculation of the spin density matrix and related quantities at leading order seems established at the most fundamental level of quantum field theory, some questions remain to be addressed. The size of higher-order terms in thermal vorticity at local equilibrium is not known, and we do not have an exact solution at global equilibrium with the density operator in Equation 8 including quantum field effects—namely, quantum statistics. Very little is known about the dissipative, non-local-equilibrium terms and their magnitude. Recently, a phenomenological approach to spin dissipation has been taken (39), generalizing a familiar classical method to constrain constitutive equations in dissipative hydrodynamics based on the positivity of entropy current divergence (40). It remains to be understood whether such a method includes all possible quantum terms in the entropy current and whether it agrees with the most fundamental quantum

approach to dissipation based on Zubarev's nonequilibrium density operator (41). Another recent study (42) has explored the possible dissipative terms of the spin tensor in the relaxation time approximation.

3.2. Hydrodynamic Calculations

The main goal of hydrodynamic calculations is to provide the key input to Equation 2: the thermal vorticity at the freeze-out hypersurface. In principle, the thermal vorticity field depends on the assumed initial conditions of the hydrodynamic calculations, on the equation of state, on the hydrodynamic constitutive equations, and on the freeze-out conditions. Nevertheless, different hydrodynamic calculations have provided similar results, and this consistency is reassuring regarding the robustness of theoretical computations of polarization.

It is important to stress that polarization studies demand a 3+1D hydrodynamic simulation. This requirement is crucial because the components of the thermal vorticity driving the projection of the mean spin vector along the total angular momentum involve the gradients of the longitudinal flow velocity, which are neglected by 2+1D codes.

A common feature of all calculations is that the values of thermal vorticity are, on average, sufficiently less than one. This feature justifies a linear approximation in the relation between mean spin vector and thermal vorticity (see, e.g., Equation 7), as shown in the histogram in **Figure 2b**. Nevertheless, a role of quadratic corrections cannot be excluded and has not been studied to date.

Several codes have been used to calculate polarization on the basis of Equation 2:

1. A 3+1D particle-in-cell simulation of ideal relativistic hydrodynamics (43); all published calculations of polarization assume peculiar initial conditions for heavy-ion collisions, implying a nonvanishing initial vorticity
2. A 3+1D code implementing relativistic dissipative hydrodynamics, ECHO-QGP (44), with initial conditions adjusted to reproduce the directed flow as a function of rapidity (45)
3. A 3+1D code implementing relativistic dissipative hydrodynamics, vHLLE (46), with initial state determined by means of a prestage of nucleonic collisions, and including a posthadronization rescattering stage, all adjusted to reproduce the basic hadronic observables in relativistic heavy-ion collisions—that is, (pseudo)rapidity and transverse momentum distributions and elliptic flow coefficients
4. A 3+1D code implementing relativistic dissipative hydrodynamics, CLVisc (47), with initial conditions provided by another transport-based simulation package, AMPT (48)

Furthermore, many calculations of polarization in the literature are based on the coarse-graining of the output provided by the transport-based simulation code AMPT (48) to obtain the thermal vorticity field in Equation 2; we refer to these calculations as transport-hybrid.

Overall, while the experimentally observed global polarization is in excellent quantitative agreement with the hydrodynamic calculations based on Equation 2, the azimuthal dependence of the polarization along angular momentum and the sign of the longitudinal component disagree with the data (see Section 4.3). These issues are discussed in Section 5.

3.3. Effects of Decays and Rescattering

Most of the calculations presented in the literature involve the primary Λs: those that are emitted from the freeze-out hypersurface. However, they are just a fraction of the measured Λs—about 25% at $\sqrt{s_{NN}} = 200$ GeV according to statistical hadronization model estimates (49)—and most of them are decay products of higher-lying states, such as Σ^0, Σ^*, and Ξ. On the basis of Equation 2,

those states also are expected to be polarized with the suitable spin-dependent coefficient (see, e.g., Equation 11)—hence, with the same momentum pattern as for the primary Λs. The secondary Λ from decays of polarized particles turns out to be polarized in turn, and its polarization vector depends on the properties of the interaction responsible for the decay (strong, electromagnetic, weak) and on the polarization of the decaying particle. The formula for the global polarization inherited by the Λs in several decay channels is shown in Reference 37, and its effect is described in Reference 50. While single channels involve a sizable correction to the primary polarization, the overall effect is small—of the order of 10% or so. This result has been confirmed by more detailed studies in which the polarization transfer in two-body decays producing a Λ hyperon was determined as a function of momentum (35, 51). Surprisingly, the combination of relative production rates of different hyperons, their decay branching ratios, and the coefficients of the polarization transfer produces an accidental cancellation of the contribution of secondary Λ polarization so that the dependence of polarization as a function of momentum is almost the same as that predicted for primary Λs alone (35, 51).

Although the contribution of secondary decays is understood, little is known about the effect of posthadronization secondary hadronic scattering after the hydrodynamic motion ceases. In general, one would expect an overall dilution of the primary polarization. However, it has been speculated (52) that final-state hadronic rescattering could generate some polarization, and Reference 53 puts forward a model showing that initially unpolarized hyperons in pA collisions can become polarized because of secondary interactions. However, applying the same model to AA collisions yields a secondary polarization consistent with zero (54).

3.4. Kinetic Models

If, for some reason, spin degrees of freedom relax more slowly than momentum, then local thermodynamic equilibrium is not a good approximation and the calculation of polarization becomes more complicated. A possible substitute theoretical approach is kinetic theory. However, as mentioned in Section 2, near the pseudocritical temperature the QGP is a strongly interacting system for which a kinetic description is dubious because the thermal wavelength of partons is comparable to their mean free path; particles interact so strongly that they are not free for most of the time. Nevertheless, one may hope that kinetic theory provides a good approximation of the spin degrees of freedom if the spin–orbit coupling is weak. However, recent estimates of the spin-flip rate in perturbative QCD indicate an equilibration time (55) that is too long, and thus nonperturbative effects seem to be essential.

A formulation of relativistic kinetic theory with spin, which dates back to the work of De Groot and collaborators (56), has been the subject of intense study over the past few years. While the development of a relativistic kinetic theory of massless fermions was motivated by the search for the chiral magnetic effect (57, 58), the corresponding theory for massive fermions has been motivated mostly by the observation of polarization. The goal of the relativistic kinetic theory of fermions is to study the evolution of the covariant Wigner function, which extends the notion of the phase space distribution function of the relativistic Boltzmann equation. For free particles, this reads as follows:

$$W(x,k)_{AB} = -\frac{1}{(2\pi)^4} \int \mathrm{d}^4 y \ e^{-ik \cdot y} \langle : \Psi_A(x - y/2)\bar{\Psi}_B(x + y/2) : \rangle, \qquad 13.$$

where Ψ is the Dirac field, A and B are spinorial indices, colons denote normal ordering, and angle brackets indicate averaging with a suitable density operator; this definition should be changed to make it gauge invariant in quantum electrodynamics. Most recent studies have aimed at a

formulation of the covariant Wigner function kinetic equations in a background electromagnetic field (59–63) at some order in $\hbar$. A different approach was taken in Reference 64, in which the polarization rate was obtained including the spin degrees of freedom in the collisional rate of the relativistic Boltzmann equation.

Kinetic theory with spin is in a theoretical development stage and has not yet produced stable numerical estimates of polarization in heavy-ion collisions. However, important steps toward this goal have been made recently. For instance, Reference 65 provides an estimate of the evolution equation of the spin density matrix in perturbative QCD. Computing tools are also being developed for the numerical solution of relativistic kinetic equations (66).

A sensitive issue regarding this approach is how to transfer the calculated polarization of partons to the hadrons (which is not relevant for the statistical hydrodynamic model; see the discussion at the beginning of this section). More generally, there is a highly nontrivial gap that needs to be bridged between the perturbative, collisional quark–gluon stage and the hadronic final state.

3.5. Spin Tensor and Spin Potential

An interesting theoretical issue concerning the description of spin effects in relativistic fluids is the possible physical separation of orbital and spin angular momentum. A similar discussion has taken place for several years in hadronic physics in connection with proton spin studies (67). A comprehensive introduction and discussion of the subject are beyond the scope of this work; we refer readers to the specialized literature (e.g., Reference 68).

In quantum field theory, the angular momentum current has, in general, two contributions: a so-called orbital part involving the stress–energy tensor and a spin part involving a rank three tensor $\mathcal{S}^{\lambda,\mu\nu}$, which is called a spin tensor. However, this separation seems to be unphysical, and one can make a transformation of the stress–energy tensor and the spin tensor to make the current all orbital, obtaining the so-called Belinfante stress–energy tensor with the total angular momentum unchanged. This transformation, which is called pseudogauge transformation (69), looks much like a gauge transformation in gauge field theories in which the stress–energy tensor and the spin tensor play the role of gauge potentials, while the total energy–momentum P^μ and angular momentum–boost $J^{\mu\nu}$ are gauge invariant. The question is whether observation of a polarization in the QGP breaks pseudogauge invariance and thus makes it possible to single out a specific spin tensor, which would be a breakthrough with remarkable consequences as it would have an impact on fundamental physics, such as relativistic gravity theories.

Indeed, the first derivation of Equation 2 made use of a specific spin tensor, which has led to some confusion even in the original paper (30). In fact, it was later observed (70) that the resulting expression of the polarization is the same regardless of the spin tensor used, among the most common choices. It has recently become clear that the definitions of spin density matrix and spin vector (71, 72) in quantum field theory do not require any angular momentum or spin operator, just the density operator and creation–destruction operators (35); thus, their expressions are completely independent of the spin tensor. In fact, the mean value of the polarization may depend on the spin tensor insofar as the density operator does. At global thermodynamic equilibrium, the density operator in Equation 8 is manifestly independent of the spin tensor because only the total angular momentum appears, but in the case of local thermodynamic equilibrium, the density operator in Equation 12 is not invariant under a pseudogauge transformation (68). In that case, in principle, one might be able to distinguish between two spin tensors by measuring the polarization. Of course, in practice, there are many uncertainties limiting the accuracy of the theoretical predictions (e.g., the hydrodynamic initial conditions), and it is not clear to what extent the measurements could solve the issue.

The inclusion of the spin tensor in relativistic hydrodynamics has been explored in some detail by Florkowski et al. in a series of papers (71, 73) and a first hydrodynamic calculation of polarization presented in a simplified boost-invariant scenario (74). As far as the heavy-ion phenomenology is concerned, a general comment is in order for the spin tensor scenario: An extended version of relativistic hydrodynamics requires six additional fields (the antisymmetric spin potential $\Omega_{\mu\nu}$), which in turn need six additional initial and boundary conditions, which are completely unknown in nuclear collisions. Polarization measurements could be used to adjust them, but doing so would strongly reduce the probing power of polarization in all other regards.

3.6. Contribution of the Electromagnetic Field

As mentioned in Section 2.1, an important feature of the statistical thermodynamic approach is that polarization is independent of the charge of the particles for a charge-neutral fluid. This fact has been confirmed by the measurements, which essentially find the same magnitude and sign for Λ and $\bar{\Lambda}$ polarization (see **Figure 3** below). Indeed, for a fluid with some charge current, a difference in the polarization of particles and antiparticles is encoded in the Fermi–Dirac distributions in Equation 2 as, for instance, the baryon chemical potential is larger at lower energy, favoring the $\bar{\Lambda}$'s polarization through the factor $n_F(1 - n_F)$ in the numerator (38). However, the known values of baryon chemical potential/temperature ratios at the relevant collision energies imply a much smaller difference in the polarization than has been observed.

A possible source of particle–antiparticle polarization splitting is the electromagnetic field, which would lead—in local equilibrium—to a modification of Equation 2, with thermal vorticity $\varpi^{\mu\nu}$ replaced by (37)

$$\varpi_{\rho\sigma} \to \varpi_{\rho\sigma} + \frac{\mu}{S}F_{\rho\sigma}, \qquad \qquad 14.$$

where μ is the particle magnetic moment. Indeed, in peripheral heavy-ion collisions, a large electromagnetic field is present at collision time, which may steer the spin vector of Λ and $\bar{\Lambda}$ and lead to a splitting of polarization since their magnetic moments are opposite.

Therefore, the polarization splitting might be taken advantage of to determine the magnitude of the electromagnetic field at freeze-out (or earlier if the relaxation time is not small) (37) or to determine its lifetime (75). Pinning down the electromagnetic field would be an important achievement in the search for local parity violation in relativistic heavy-ion collisions (76) through the so-called chiral magnetic effect (57, 58). However, alternative explanations of the splitting have been proposed, and this feature needs to be explored experimentally and theoretically. We return to this issue below in Section 5.2.

4. POLARIZATION IN RELATIVISTIC HEAVY-ION COLLISIONS: OBSERVATIONS

To date, there have been few measurements of spin polarization in relativistic heavy-ion collisions. These measurements require excellent tracking and vertex resolution in the region of interest (typically midrapidity), large coverage and good particle identification to measure decay products, high statistics to measure relatively small correlation signals, and a suite of detectors to correlate forward-rapidity momentum anisotropies with midrapidity decay topologies. Several such experiments are ongoing, and more will soon be commissioned. The initial measurements described here will eventually be part of a fuller set of mapped systematics.

4.1. Measuring Polarization

If spin is locally equilibrated, as discussed above, all hadrons with spin will be polarized. However, while polarimeters (77) may directly detect the polarization of particles in very clean environments, their use is infeasible in a final state that involves thousands of hadrons.

Recording the debris from the midrapidity region in a heavy-ion collision usually involves large tracking systems (e.g., 78). A particle's polarization may be determined by the topology of its decay into charged particles if the angular distribution of the daughters' momenta is related to the spin direction of the parent.

For weak parity-violating hyperon decays with spin and parity $\frac{1}{2}^+ \rightarrow \frac{1}{2}^+ + 0^-$, the daughter baryon is emitted preferentially in the direction of the polarization vector $(\mathbf{P}_H^*)$ of the parent as (79)

$$\frac{dN}{d\Omega^*} = \frac{1}{4\pi}(1 + \alpha_H \mathbf{P}_H^* \cdot \hat{\mathbf{p}}_D^*) = \frac{1}{4\pi}(1 + \alpha_H \cos\xi^*), \qquad 15.$$

where $\hat{\mathbf{p}}_D^*$ is a unit vector pointing in the direction of the daughter baryon momentum, and ξ^* is the angle between $\hat{\mathbf{p}}_D^*$ and the polarization direction. Here and throughout, asterisks denote quantities as measured in the rest frame of the decaying parent. The decay parameter α_H depends on the hyperon species (80).

The general task in extracting polarization from experimental data is to identify a potential direction—say, $\hat{\mathbf{n}}$ (specific examples are discussed below). The ensemble-averaged projection of the daughter baryon's momentum along $\hat{\mathbf{n}}$ gives the projection of $\mathbf{P}$:

$$\langle \hat{\mathbf{p}}_D^* \cdot \hat{\mathbf{n}} \rangle = \frac{\alpha_H}{3} \mathbf{P}_H^* \cdot \hat{\mathbf{n}}. \qquad 16.$$

First measurements (7, 26, 81–83) of polarization in relativistic heavy-ion collisions have used $\Lambda \rightarrow p + \pi^-$ ($\bar{\Lambda} \rightarrow \bar{p} + \pi^+$) decays. The decay parameter for an antiparticle is expected and observed (80, 84) to be of equal magnitude and opposite sign to the corresponding particle within measurement uncertainties.[4]

Polarization of other hadronic species may also be measured in principle. The reduced efficiency associated with identifying two displaced vertices, as well as the reduced yield of doubly strange baryons, makes using Ξ^- ($\alpha_{\Xi^- \rightarrow \Lambda + \pi^-} = -0.458$) more difficult. The neutral decay of Ξ^0 ($\alpha_{\Xi^0 \rightarrow \Lambda + \pi^0} = -0.406$) is more difficult still. Relatively low production rates (86) and very small α_Ω values (80) strongly disfavor the use of triply strange Ω baryons.

For spin $\frac{1}{2}$ particles, polarization is entirely described by the mean spin vector, which has been extensively discussed in this review. For particles with spin $> \frac{1}{2}$, a full description of the polarization state requires more quantities; in practice, one should quote the full spin density matrix $\Theta_{rs}(p)$ (see Section 3). In particular, for spin 1 particles, a quantity independent of the mean spin vector related to the polarization state is the so-called alignment (87):

$$A = \Theta_{00}(p) - 1/3.$$

---

[4]Until very recently, the accepted world average value (80) was $\alpha_\Lambda = 0.642 \pm 0.013$. However, recent measurements (e.g., 84) have led to a new accepted value (85) of $\alpha_\Lambda = 0.732 \pm 0.014$, a change of about 6σ. Although the source of this significant discrepancy between earlier and more recent measurements is not entirely clear, we follow the Particle Data Group and adopt the new value. Therefore, we have decided to rescale all reported polarizations to reflect the currently accepted value of α_Λ.

A randomly oriented ensemble would have $\Theta_{00} = \frac{1}{3}$ and hence vanishing A; a value of $\Theta_{00} \neq \frac{1}{3}$ indicates spin alignment, though by symmetry it is impossible to distinguish the sign in $\langle \mathbf{S} \rangle \parallel \hat{\mathbf{n}}$. The two-particle decay topology of a vector meson is related to the alignment according to the following equation (88):

$$\frac{\mathrm{d}N}{\mathrm{d}\cos\xi^*} = \frac{3}{4}[1 - \Theta_{00} + (3\Theta_{00} - 1)\cos^2\xi^*], \qquad 17.$$

where ξ^* is defined as in Equation 15. At local thermodynamic equilibrium, $\frac{1}{3} - \Theta_{00}$ is quadratic in thermal vorticity to first order, as mentioned in Section 3.

Thus far, the first measurements of global spin alignment of vector mesons in heavy-ion collisions are difficult to understand in a consistent picture. We discuss this issue in Section 5.3; here, we focus on hyperon polarization.

4.2. Global Hyperon Polarization: Observation

By symmetry, the average vorticity of the QGP fireball must point in the direction of the fireball's angular momentum $\mathbf{J}_{\mathrm{QGP}}$, and on average $\mathbf{J}_{\mathrm{QGP}} \parallel \mathbf{J}_{\mathrm{sys}}$ (see **Figure 1**). Similarly, even without appealing to a connection to vorticity, when averaged over all particles symmetry demands an average (over all emitted particles) polarization aligned with $\hat{\mathbf{J}}_{\mathrm{sys}}$. In the current context, the global polarization of a subset of particles refers to the use of $\hat{\mathbf{n}} = \hat{\mathbf{J}}_{\mathrm{sys}}$ in Equation 16.

As discussed in Section 2.2, the momentum-space anisotropy of particle emission is used (22) to extract an event plane angle $\Psi_{\mathrm{EP},1}$ which approximates the reaction plane with some finite resolution. Standard methods have been developed (22) to correct for the effects of this resolution on measured asymmetries in the emission pattern about the beam axis, so it is convenient to rewrite Equation 16 as[5] (26)

$$P_{H\hat{\mathbf{j}}} = \frac{3}{\alpha_H}\langle \hat{\mathbf{p}}_{\mathbf{D}}^* \cdot (\hat{\mathbf{b}} \times \hat{\mathbf{p}}_{\mathrm{beam}}) \rangle = \frac{3}{\alpha_H}\langle \cos\xi^* \rangle = -\frac{3}{\alpha_H}\langle \sin(\phi_D^* - \Psi_{\mathrm{RP}})\sin\theta_D^* \rangle. \qquad 18.$$

Here, ϕ_D^* and θ_D^* are the angles between the daughter momentum and $\hat{\mathbf{b}}$ and $\hat{\mathbf{p}}_{\mathrm{beam}}$, respectively, and in the last step, a trigonometric relationship between the angles is used. These angles are shown in **Figure 3**.

Integrating[6] over polar angle θ_D^* yields the following:

$$P_{H\hat{\mathbf{j}}} = -\frac{8}{\pi\alpha_H}\langle \sin(\phi_D^* - \Psi_{\mathrm{RP}}) \rangle = -\frac{8}{\pi\alpha_H R_{\mathrm{EP}}^{(1)}}\langle \sin(\phi_D^* - \Psi_{\mathrm{EP},1}) \rangle, \qquad 19.$$

where in the final step, the experimentally determined event plane angle replaces the reaction plane angle, accounting for the resolution with a calculable correction factor $R_{\mathrm{EP}}^{(1)}$ (22).

The resolution with which $\hat{\mathbf{J}}_{\mathrm{sys}}$ is measured is critical. Polarization affects daughter anisotropies only at a level of a few percent, and statistical uncertainties can dominate experimental results.

---

[5]For a discussion of significant experimental challenges in performing the averaging shown in Equation 18, readers are referred to Reference 93.

[6]Detectors in which Λs are reconstructed usually do not measure the charged daughters at very forward angles at collider energies. To account for this, corrections (26, 94) on the order of $\sim$3% (93) are applied.

Using Equation 19, the statistical uncertainty on polarization is

$$\delta P_{H\hat{\mathbf{J}}} \sim \left(R_{\mathrm{EP}}^{(1)} \cdot \sqrt{N_H} \right)^{-1}, \qquad\qquad 20.$$

where N_H is the total number of hyperons analyzed in the data set. This dependence is generically true for any measurement that involves correlation with the first-order event plane or $\hat{\mathbf{J}}_{\mathrm{sys}}$. Increasing the resolution by a factor of two (95) thus decreases the required duration of an experimental campaign fourfold.

Figure 3 shows the world data set of $P_{\Lambda\hat{\mathbf{J}}}$ and $P_{\bar{\Lambda}\hat{\mathbf{J}}}$ as a function of collision energy for semiperipheral collisions. As discussed in Section 4.1, the recent change in accepted value for α_Λ requires a rescaling of the published experimental values. From a maximum of $\sim$1.5% at $\sqrt{s_{NN}} = 7.7$ GeV, the polarizations fall smoothly[7] with energy. At LHC energies, they vanish within experimental uncertainties.

Strikingly, all available hydrodynamic and transport calculations reproduce the observations in sign, magnitude, and energy dependence, as discussed in Section 3.2. This fact is nontrivial; because these calculations all use Equation 2, they all predict a similar thermal vorticity field. These models have been tuned to some extent to reproduce earlier observations such as anisotropic flow (6), which is sensitive to the bulk motion of fluid cells from which particles emerge; it is thus satisfying that they produce similar and correct predictions for this more sensitive observable.

Clearly, $|\mathbf{J}_{\mathrm{sys}}|$ increases with increasing $\sqrt{s_{NN}}$, and transport calculations (96, 97) predict that about 20% of this angular momentum is transferred to the QGP fireball. While some early calculations (25) predicted an increased polarization at high collision energies, a strongly decreasing trend is produced by most hydrodynamic (50, 98) and transport-hybrid codes in which the thermal vorticity field is obtained through a coarse-graining procedure (96, 99–102).

Driving mechanisms may include increased temperature (103) at increased $\sqrt{s_{NN}}$; increases in evolution timescale (50, 91); vorticity migrating to forward rapidity (28, 92, 96), perhaps due to reduced baryon stopping and/or increased transparency at high energy (50); an increased fluid moment of inertia due to increased mass energy (96); and reduced longitudinal fluctuations and boost invariance at high energy (104).

In addition to the overall energy dependence, the data in **Figure 3** suggest a fine splitting between particles and antiparticles at low $\sqrt{s_{NN}}$. While statistically not significant at any given energy, important physical effects are predicted to manifest in $P_{\bar{\Lambda}\hat{\mathbf{J}}} > P_{\Lambda\hat{\mathbf{J}}}$, as we discuss in Section 5.2.

Even as we note possible differences between the polarizations of Λ and $\bar{\Lambda}$, it is clear that to good approximation they are the same even at the lowest energies, suggesting similar average vorticity of the cells from which they arise. This similarity is remarkable given that the directed flow of these particles diverges strongly (105) as the energy is reduced below $\sqrt{s_{NN}} \approx 20$ GeV, even taking opposite signs at midrapidity. In the hydrodynamic paradigm, directed flow (22)—essentially the sideward push of forward-going particles (see **Figure 1**)—reflects the anisotropy of the bulk fluid velocity about the $\hat{\mathbf{J}}$ axis at a large scale. Meanwhile, global polarization reflects rotational flow structure about $\hat{\mathbf{J}}$ at a more local scale. There may be a coupling in a hydrodynamic picture (12, 103, 106). Whether there is a tension here is unclear, though a three-fluid hydrodynamic code is able to approximately reproduce proton and antiproton flow (107) and Λ polarization (92).

---

[7]While eye-catching, the value of $P_{\bar{\Lambda}\hat{\mathbf{J}}} = (7.4 \pm 3.1)\%$ at the lowest energy is less than 2σ above the general systematics and is marginally significant.
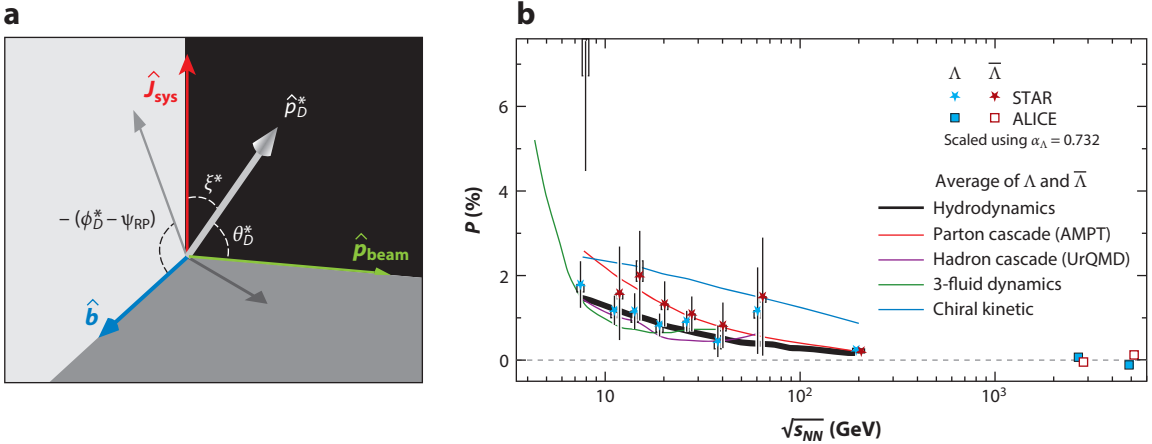
Figure 3

(*a*) The vectors and angles involved in an analysis of hyperon polarization along the angular momentum of the collision. In the lab coordinate system (not shown), the azimuthal angle of $\hat{\mathbf{b}}$ is defined as Ψ_{RP}. Thus, the angle between the projection of $\hat{\mathbf{p}}_D^*$ and $\hat{\mathbf{b}}$ is $\phi_D^* - \Psi_{RP}$. The minus sign on the indicated angle reflects the fact that azimuthal angles are measured counterclockwise about the beam axis. (*b*) The energy dependence of Λ and $\bar{\Lambda}$ global polarization at midrapidity from midcentral Au+Au (20–50%) or Pb+Pb (15–50%) collisions. Data (7, 26, 81, 83) are compared with polarization simulations of viscous hydrodynamics (50), partonic transport (89), hadronic transport (90), chiral-kinetic transport plus coalescence (91), and a three-fluid hydro model applicable at lower energies (92). Experimental data points have been corrected for the recent change in α_Λ, as discussed in Section 4.1. For viscous hydrodynamics (50) and partonic transport (89), the values shown represent both primary and feed-down hyperons (cf. Reference 37).

4.3. Global and Local Polarization at $\sqrt{s_{NN}} = 200$ GeV

To date, systematic studies of the dependence of $P_{\hat{\mathbf{j}},H}$ in Au+Au collisions have been possible only at $\sqrt{s_{NN}} = 200$ GeV (81). Statistics are poor at low energies, while at higher energies the signal itself vanishes. More detailed measurements can pose stringent challenges to theoretical models and may provide new insight. In collisions at $\sqrt{s_{NN}} = 200$ GeV, polarizations of Λ and $\bar{\Lambda}$ are identical within uncertainties, so in this section we discuss their average.

In **Figure 3**, global hyperon polarization is shown for collisions with a centrality of 20–50% (see Section 2.2), corresponding to $|\mathbf{b}| \approx 7$–11 fm. **Figure 4** shows the centrality dependence. Both the global polarization and the oscillation of the longitudinal local polarization (see Section 4.3) increase monotonically with impact parameter, as expected for a phenomenon driven by bulk mechanical angular momentum; this finding is in agreement with transport-hybrid calculations (96).

The global polarization—that is, the polarization integrated over all particles at midrapidity—is nonzero and aligned with an event-specific direction.[8] Momentum-differential (local) polarization structures, in the local equilibrium picture, are more sensitive to the thermal vorticity variations as a function of space and time, convoluted with flow-driven space–momentum correlations. The first measurements (81) reported $P_{\hat{\mathbf{j}},\Lambda/\bar{\Lambda}}$ to be independent of transverse momentum for $p_T \lesssim 2$ GeV/c, in agreement with hydrodynamic predictions (12, 110) that assume

---

[8]This fact is in strong contrast to the well-known phenomenon (108, 109) in *pp* and *pA* collisions, in which Λ (but not $\bar{\Lambda}$, for unclear reasons) hyperons emitted at very forward angles are polarized along their production plane, spanned by $\mathbf{p}_\Lambda \times \mathbf{p}_{\text{beam}}$. This effect is rapidity-odd and vanishes at midrapidity. In principle, convolution of the production plane polarization with finite directed flow (22) could produce a global effect. However, in practice, this effect is much smaller than those we discuss here (31).
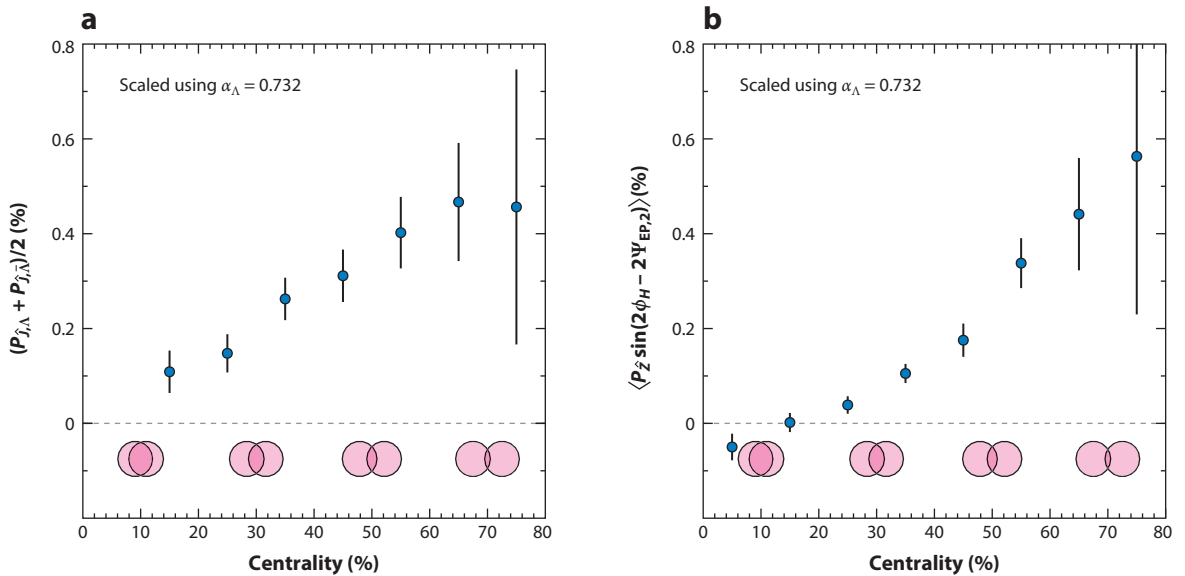
Figure 4

Centrality dependence of hyperon (average of Λ and $\bar{\Lambda}$) polarization in Au+Au collisions at 200 GeV. As in **Figure 3**, published data have been rescaled to reflect the new accepted value of α_Λ. The pink circles at the bottom of each panel roughly sketch the geometry of the overlap region for a given centrality. (*a*) Global polarization (81). (*b*) Second-order oscillation amplitude of the longitudinal polarization (82).

realistic initial conditions. It was also seen (81) to be independent of pseudorapidity, though only a limited range (i.e., $|\eta| < 1$) could be explored. As we discuss in Section 5, several theories suggest that much could be learned at forward rapidity.

A recurring theme in heavy-ion physics is that azimuthal dependencies often present surprises and the opportunity for new physical insight. The same may be true for polarization. **Figure 5** shows preliminary data from the STAR Collaboration (111) that suggest that $P_{\mathbf{J},\Lambda/\bar{\Lambda}}$ is significantly stronger for particles emitted perpendicular to $\hat{\mathbf{J}}_{\mathrm{sys}}$ ($|\phi_\Lambda - \Psi_{\mathrm{RP}}| = \pi/2$) than for $\hat{\mathbf{p}}_\Lambda \parallel \hat{\mathbf{J}}$. Indeed, $P_{\mathbf{J}}$ may vanish for hyperons emitted out of the reaction plane. This observation stands in contradiction to rather robust predictions of hydrodynamic (12, 31, 50, 98, 112) and coarse-grained transport (96, 100–102) calculations (one of which is shown in **Figure 5b**), which predict precisely the opposite dependence. If the STAR results are confirmed in a final analysis, this finding will represent a nontrivial challenge to the theory.

By symmetry, polarization components perpendicular to $\hat{\mathbf{J}}_{\mathrm{sys}}$ must vanish when averaging over all momenta. Locally in momentum space, however, these components are allowed to be nonvanishing. In particular, there can be nonvanishing values oscillating as a function of the azimuthal emission angle ϕ_H over the transverse plane with a typical quadrupolar pattern. Hydrodynamic (12) and transport calculations (100) predict the sign and magnitude of these oscillations. Here, $\hat{\mathbf{n}} = \hat{\mathbf{p}}_{\mathrm{beam}}$ in Equation 16, so $\xi_D^* = \theta_D^*$, the polar angle of the daughter in the hyperon frame (see **Figure 3**).

Hydrodynamic (12, 50, 110, 112) and transport-hybrid (96, 100–102) calculations predict a negative sign of the longitudinal component of the polarization vector in the first quadrant of the $\mathbf{p}_T$ plane rotating counterclockwise from the reaction plane. One such calculation is shown in **Figure 6b**, while the corresponding measurement (82) is shown in **Figure 6a**. The magnitude
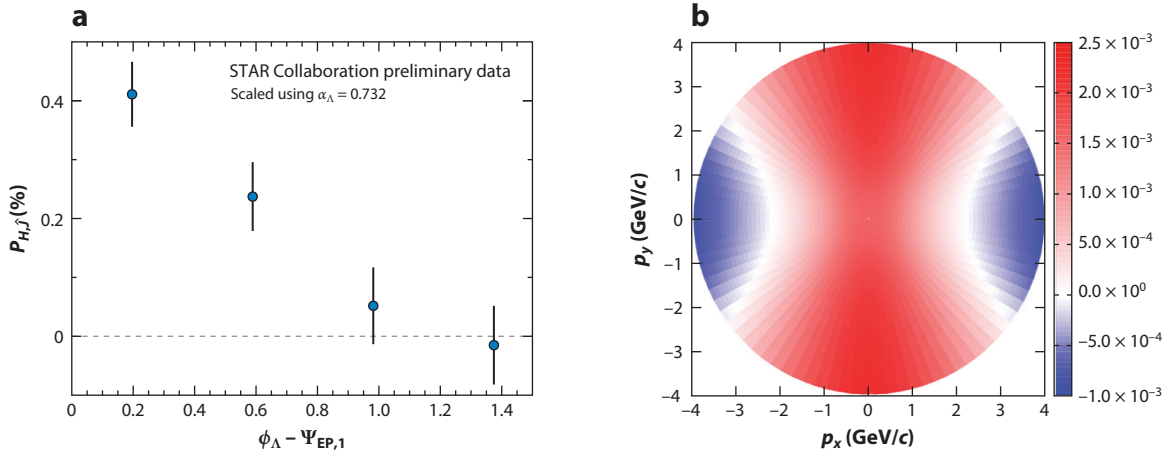
Figure 5

(*a*) Preliminary results (111) from the STAR Collaboration for the global polarization of Λ and $\bar{\Lambda}$ as a function of hyperon emission angle relative to the event plane, for midcentral Au+Au collisions at $\sqrt{s_{NN}} = 200$ GeV. As in **Figure 3**, published data have been rescaled to reflect the new accepted value of α_Λ. (*b*) Hydrodynamic calculations of $P_{\hat{\mathbf{j}}}$ in the transverse momentum plane for the same colliding system. The horizontal axis $p_y = 0$ corresponds to the angle $\phi_\Lambda - \Psi_{\mathrm{EP},1} = 0$ in panel *a*, whereas the axis $p_x = 0$ in panel *b* corresponds to $\phi_\Lambda - \Psi_{\mathrm{EP},1} = \pi/2$. Panel *b* adapted with permission from Reference 12.

of the effect is significantly larger in the model, but more strikingly, the sign of the predicted oscillation is opposite that seen in the data, reminiscent of the discrepancy in **Figure 5**.

Understanding and resolving the tension in **Figures 5** and **6** is among the most pressing open issues in this area. We discuss this issue further in Section 5.
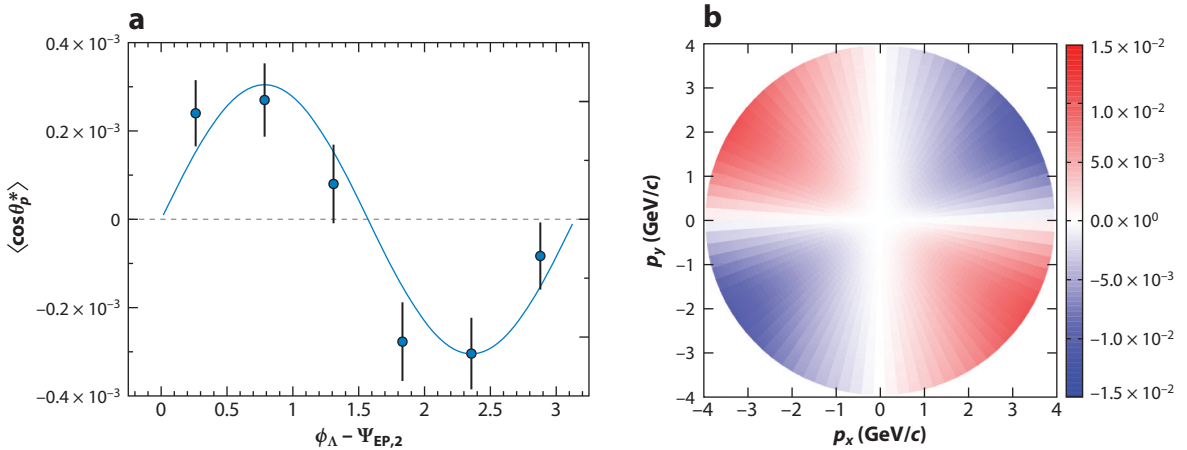

Figure 6

The $\langle \cos \theta_p^* \rangle$ values for 20–60% centrality Au+Au collisions at $\sqrt{s_{NN}} = 200$ GeV as a function of hyperon emission angle relative to the event plane (82). Small detector effects (see Footnote 6) and event plane resolution effects have not been corrected for in the figure. (*a*) A sinusoidal curve is drawn to guide the eye. (*b*) Hydrodynamic calculations of $P_{\hat{\mathbf{z}}}$ in the transverse momentum plane for the same colliding system. The horizontal axis $p_y = 0$ corresponds to the angle $\phi_\Lambda - \Psi_{\mathrm{EP},2} = 0$ in panel *a*, whereas the axis $p_x = 0$ in panel *b* corresponds to $\phi_\Lambda - \Psi_{\mathrm{EP},2} = \pi/2$. Starting from $p_y = 0$ and increasing to positive p_y (i.e., to positive $\phi_\Lambda - \Psi_{\mathrm{EP},2} = 0$), hydrodynamic calculations predict that the longitudinal polarization sign will become negative. Panel *b* adapted with permission from Reference 12.

5. OPEN ISSUES AND OUTLOOK

Above, we have presented the theoretical framework (mostly hydrodynamics) in which to calculate the vorticity of the QGP; the theoretical connection between the vorticity and the polarization of hadrons emitted from the plasma, based on local thermodynamic equilibrium of hadrons and their generalized distribution function; and the measurements of this polarization with Λ hyperons. Overall, the hydrodynamic and statistical equilibrium paradigm has predicted the first experimental observations of global polarization strikingly well.

However, qualitative discrepancies between theory and experiment may indicate that some fundamental feature of the dynamics itself (encoded hydro or transport) is misunderstood or unaccounted for. Alternatively, we may misunderstand the interface (Cooper–Frye and thermal vorticity) between hydrodynamics or its coarse-grained approximation and the polarization observable. Clearly, the existing data demand more theoretical work; Section 5.1 provides a report on the recent and ongoing work on this topic. There also are many important theoretical predictions that demand experimental tests. Such testing will involve new detectors, future facilities, and new analysis techniques.

Finally, two topics deserve separate attention. One is the possibility that polarizations of Λ and $\bar{\Lambda}$ are different. The other concerns the spin alignment of vector mesons.

5.1. Local Polarization

The discrepancies between hydrodynamic calculations and the polarization pattern in momentum space, which are presented in Section 4.3, have been the subject of investigations over the past year. The simplest explanation—that these discrepancies are an effect of secondary decays (see Section 3.3)—has been ruled out (35, 51); the secondary Λs have almost the same momentum dependence of the polarization as do the primary Λs, if all primary particles are polarized according to the hydrodynamic predictions. The other simple explanation is a polarization change in posthadronization rescattering, which is not taken into account in simulation codes; however, such a change seems very unlikely (see discussion in Section 3.3), especially because it should produce an amplification in some selected momentum regions. The available hadronic transport codes do not include the spin degrees of freedom mostly because the helicity-dependent scattering amplitudes are unknown, and even if one resorts to educated guesses, it is a formidable computational task to include them in Monte Carlo codes.

Within the hydrodynamic paradigm, there are more options yet to be explored. The first involves Equation 2, which is first order in thermal vorticity. Indeed, thermal vorticity is moderately smaller than one (see **Figure 2**), and the exact formula at all orders is not known yet, so a sizable role of higher-order corrections cannot be ruled out for the present.

Because polarization is steered by thermal vorticity, it is possible that the thermal vorticity field is different from the predictions obtained with the presently used initial hydrodynamic conditions, tuned to reproduce a set of observables in momentum space. Recently, Xie et al. (113) obtained the right sign of the longitudinal polarization at $\sqrt{s_{NN}} = 200$ GeV with specific initial conditions (114); the same model predicts the wrong sign at lower energy (i.e., $\sqrt{s_{NN}} = 8$ GeV) (112).

Another possibility is that spin dissipative corrections (analogous to viscous corrections for the stress–energy tensor), which are not included in the local thermodynamic equilibrium assumption, are sizable. As mentioned in Section 3, the theory of dissipation and spin in a hydrodynamic framework has recently drawn the attention of several authors; as yet, it is not clear whether such an approach includes relevant quantum terms and whether it is pseudogauge dependent (see Section 3.5).

Furthermore, it has been considered that other kinds of vorticity, instead of thermal vorticity (Equation 3), enter into the polarization definition. In Reference 102, it has been shown that the right sign of the longitudinal polarization is retrieved if the thermal vorticity is replaced by a tensor proportional to the T-vorticity (12), whereas in Reference 115 the agreement is restored by replacing the thermal vorticity with its double projection perpendicular to the velocity field. So far, these observations are not borne out by fundamental theoretical justifications.

Finally, it should be mentioned that in Reference 116, the correct polarization patterns have been obtained for the polarization of quarks within a chiral kinetic model; the question remains on the effect of hadronization.

If none of the approaches described above adequately describes the data, two scenarios may be envisioned:

- spin does not locally equilibrate and has to be described within a kinetic approach (see Section 3.4); or
- spin equilibrates locally, but pseudogauge invariance is broken, and one needs a spin potential to describe its hydrodynamic evolution with six additional degrees of freedom and six additional hydrodynamic equations (see Section 3.5).

Of course, both of these scenarios should explain why the global polarization is in very good agreement with local equilibrium with thermal vorticity. Finally, there may be some important factor(s) that has not yet been considered.

5.2. Λ-$\bar{\Lambda}$ Splitting

As discussed above, while the difference is statistically insignificant at any given energy, $P_{\bar{\Lambda},J}$ is systematically larger than $P_{\Lambda,J}$ at the lower collision energies at which polarization itself is large. A possible interpretation of such a splitting is the presence of a large electromagnetic field, and one could use the observed difference to extract the value of the magnetic field in the rest frame of the particles, as discussed in Section 3.6.

To first approximation, the $\hat{\mathbf{J}}$-component of the vorticity is determined by the sum of $P_{\Lambda,J}$ and $P_{\bar{\Lambda},J}$, and the value of the magnetic field is determined by their difference (37). However, feed-down corrections can be important and should be accounted for (37). For example, in the absence of feed-down, a finite B-field would produce $P_{\bar{\Lambda},J} > P_{\Lambda,J}$, and $B = 0$ would result in no difference in the polarizations. However, if $B = 0$, then feed-down effects at low collision energies (where there are significant chemical potentials at freeze-out) can generate a splitting with opposite signs—that is, $P_{\bar{\Lambda},J} < P_{\Lambda,J}$ (37). Applying Equation 2 (with the substitution from Equation 14) to the data in **Figure 3**, accounting for feed-down effects (37), results in an estimate of $B = (6 \pm 6) \times 10^{13}$ T when averaging over results from $10\,\mathrm{GeV} < \sqrt{s_{NN}} < 40\,\mathrm{GeV}$. Such an average is hardly justified, but it nevertheless provides a valuable estimate of the magnitudes of the magnetic field—and the measurement uncertainty—that may be associated with the data. In the equilibrium paradigm, this estimate represents the magnetic field at freeze-out. Theoretically, fields of this magnitude are present in the first instants of a heavy-ion collision. Although they may decay well before freeze-out, a highly conductive QGP itself can significantly extend the lifetime of the initially large field (117), and vorticity certainly helps in this respect (118). At low $\sqrt{s_{NN}}$, field lifetimes may be longer (119) and QGP evolution times shorter. Relativistic magnetohydrodynamics is the standard tool by which to study the evolution of the electromagnetic field in a plasma, and there have been major advances recently (120, 121). If feed-down corrections are neglected, the similarity of $P_{\Lambda,J}$ and $P_{\bar{\Lambda},J}$ (122) places an upper limit on the magnetic field at freeze-out of about 10^{12} T at top RHIC energy. Measurements by the STAR Collaboration in the second phase of

the RHIC Beam Energy Scan (BES-II) will have an order of magnitude better statistics (123) and better event plane resolution (95), which will enable much tighter limits on the field and may provide evidence for it.

Transport calculations may provide more insight with respect to local thermodynamic equilibrium. Simplified calculations estimate that the expected field could be on the order of 10^{12} to 10^{13} T, and the energy dependence of the splitting would resemble that seen in the data (118). A more sophisticated calculation (75) with partonic transport suggests that the difference between $P_{\Lambda, J}$ and $P_{\bar{\Lambda}, J}$ may be reasonably attributed to the accumulated effect of an evolving magnetic field—interestingly, in the absence of a magnetic field, $P_{\bar{\Lambda}, J} < P_{\Lambda, J}$.

A firm statement on the existence of a long-lived (several fm/c) magnetic field on the scale of 10^{13} T would have tremendous implications for the chiral magnetic effect (57). However, several effects have been postulated, which may complicate the interpretation of the splitting. Especially at low collision energies, at which baryon stopping is significant, Λ and $\bar{\Lambda}$ may originate from different regions within the fireball (90), and their final polarizations would thus reflect differently weighted averages over vorticity. Han & Xu (124) argue that the quark–antiquark vector potential in the presence of the net quark flux at these energies may generate a splitting that is largely indistinguishable from that expected from a magnetic field. The vector meson field may play an equivalent role in the hadronic sector; however, existing calculations (125, 126) reproduce the splitting only by adjusting by hand the unknown sign, magnitude, and energy dependence of the effect.

In principle, disentangling these effects could require a full 3D magnetohydrodynamic calculation that includes appropriate vector potentials, conserved nontrivial baryon currents, and QGP conductivity, potentially followed by a hadronic cascade with spin-transfer collisional dynamics. Hopefully, sophisticated but achievable calculations, in conjunction with targeted measurements, can lead to reasonable estimates of the individual contributions of these important effects.

5.3. Alignment

In peripheral collisions, the anisotropy generated by the collective angular momentum implies that all particles with spin can, in principle, have a nonvanishing polarization. In particular, for vector mesons this implies a nonvanishing alignment, as discussed in Section 4.1. At local thermodynamic equilibrium, Equation 10 predicts an alignment that is quadratic in the thermal vorticity (29). Because thermal vorticity is less than one throughout (see **Figure 2**), and because at freeze-out it is on the order of 0.02, the expected resulting alignment is tiny.

In fact, preliminary results regarding the alignment have been reported for two vector mesons, K^* and ϕ, at RHIC (127) and LHC (128). In all cases, Θ_{00} (see Equation 17) is considerably different from $\frac{1}{3}$. For ϕ at LHC and K^* at both colliders, the measured values would imply a vorticity at least two orders of magnitude higher than calculations or expectations from the hyperon measurements. More surprisingly, Θ_{00} for the ϕ mesons at RHIC is greater than $\frac{1}{3}$ (127)—a finding that cannot be understood in the hydrodynamic or recombination model (129). This observation may require fundamentally new physics mechanisms (130) for alignment that apply at RHIC but not at LHC. Altogether, the situation with these preliminary spin alignment measurements is not sufficiently understood to discuss in a review.

5.4. Future Measurements

As we have discussed, the first few positive observations of hyperon polarization at RHIC have generated tremendous theoretical activity. Much of this work has focused on the degree to which

models can reproduce the measurements, but a growing body of work points to the ways in which new measurements can strictly test our understanding of QGP dynamics and may provide enhanced sensitivity to important physics.

5.4.1. Measurements underway.

The STAR Collaboration is engaged in the second phase of the RHIC BES-II, which will have an order of magnitude better statistics (123) and better event plane resolution (95) than has been achieved so far in collisions at $\sqrt{s_{NN}} \lesssim 30$ GeV. These measurements will soon place a much tighter bound on the magnetic field at energies at which the field may last longer and the freeze-out may occur earlier. They also will more tightly test the validity of hydrodynamics under conditions of large baryochemical potential.

The high-statistics data sets taken by the STAR Collaboration are also being reanalyzed to explore possible Ξ polarization. Measurement with an additional particle will be extremely useful to test the validity of the equilibrium description described in this review. It will be equally important to finalize the preliminary analysis shown in **Figure 5**.

5.4.2. Lower-energy collisions.

As shown in **Figure 3**, both the observed and predicted polarization signals rise as the collision energy is reduced. Exploring this trend for even lower energies may touch on several important questions: Does a hydrodynamic description of the system break down at lower energy density? What are the effects of increased viscosity (50, 131–133)? Can spin equilibrate rapidly enough to justify a local thermodynamic equilibrium approximation—and if so, is this due to hadronic mechanisms or to the QCD phase transition? Some hydrodynamic models tuned for low energies predict an uninterrupted continued rise (103, 112) regardless of equation of state (92, 134), though initial-state and thermalization assumptions may affect this behavior at the lowest energies, producing a nonmonotonic behavior (135).

In Section 4.2 above, we have remarked on the possible tension between Λ and $\bar{\Lambda}$ directed flow and polarization at low collision energy; how tightly coupled are the large-scale and smaller-scale rotational structures in the flow fields probed by these particles? It has been suggested (107, 136) that the diverging behavior of baryon and antibaryon directed flow (105, 137) signals a phase transition in the equation of state. Alternatively, this diverging behavior may arise from a convolution of baryon stopping and quark coalescence (105, 138).

Again regarding Λ and $\bar{\Lambda}$, it has been suggested (90) that differences in polarization are dominated by differences in the phase space from which these particles arise; such differences are largest at low collision energy. Of course, testing this hypothesis and that discussed in the previous paragraph will require measurement of local polarization—that is, as a function of momentum.

Addressing these questions will require new measurements at $\sqrt{s_{NN}} \lesssim 10$ GeV with good tracking, event plane resolution, and high statistics, especially given plummeting $\bar{\Lambda}$ yields. Such measurements will be pursued at the future NICA (139, 140) and FAIR (141) facilities (2 GeV $\lesssim \sqrt{s_{NN}} \lesssim 11$ GeV) as well as in the STAR/RHIC fixed-target program (142) and the HADES/GSI experiment (143).

5.4.3. Measurements at forward rapidity.

Thus far, polarization has been measured at midrapidity to focus on the hottest part of the QGP fireball. However, calculations with a variety of models suggest a vortical structure that evolves with rapidity.

A geometric calculation (28) based on the BGK model of hadron production (144) and boost invariance suggests that vorticity will increase with rapidity and that a rapid change in the evolution could signal a phase change at some critical density. A similar, more recent calculation (145) finds that the rapidity dependence of vorticity itself depends on $\sqrt{s_{NN}}$ at RHIC energies and that

it is sensitive to important physical parameters of the model itself. Numerical calculations with transport-hybrid codes (96, 99, 102) also indicate a forward migration of vorticity, especially as the collision energy increases (99). Finally, hydrodynamic models predict much higher vorticity in the beam fragmentation region at both NICA (97, 146) and RHIC (92, 147) energies.

Exploring vorticity away from midrapidity in fixed-target experiments (discussed above) is relatively straightforward. At collider energies, the STAR forward upgrade will provide coverage and tracking over a physically important region (145). If the event plane can be reconstructed, the LHCb experiment (148) could be used to explore the rapidity evolution at the highest energies.

5.4.4. Other polarization projections.

Experiments have reported polarization projections along $\hat{\mathbf{n}} = \hat{\mathbf{J}}$ and $\hat{\mathbf{n}} = \hat{\mathbf{p}}_{\text{beam}}$ (see Equation 16). The geometry of the collision itself suggests other natural directions.

For particles emitted at forward rapidity, symmetry permits an average polarization projection along $\hat{\mathbf{n}} = \hat{\mathbf{b}}$. In fact, so-called vortex rings or cyclones are predicted (100, 147) at forward rapidity at RHIC (100) and NICA (97, 147) energies (4 GeV $\lesssim \sqrt{s_{NN}} \lesssim$ 11 GeV) as well as at midrapidity in nonsymmetric systems (149). In this case, $\hat{\mathbf{n}} \parallel \mathbf{p}_\Lambda \times \hat{\mathbf{z}}$.

One of the first model studies of vorticity in heavy-ion collisions predicted similar ring-like structures relative to jets. High-momentum partons that are formed in the initial stages of the heavy-ion collision lose energy in the QGP fireball (150) and can locally perturb the flow field (151). This process may produce a cone or ring of vortical structure locally perpendicular to the direction of the deposited momentum (28), $\hat{\mathbf{n}} = \hat{\mathbf{p}}_{\text{dep}} \times \hat{\mathbf{p}}_H$, where the hyperon H has acquired an outward velocity from the radial flow (6) of the QGP.

Finally, the QGP depicted in **Figure 1** is likely to be characterized by turbulence (106, 152, 153), in which the vorticity of a fluid cell is not correlated with a global event characteristic or symmetry-breaking direction. However, the assumption is that the polarizations of all particles emitted from a cell are aligned with the vorticity of that cell and that flow-induced space–momentum correlations (6) cause particles from the same cell to be emitted in the same direction. Hence, if experimental complications can be overcome, spin–spin correlations as a function of relative momentum (or angle) are a promising way to probe the turbulent vortical substructure of the QGP (104).

6. SUMMARY

Polarization has opened an exciting new direction in relativistic heavy-ion physics—one of the increasingly rare truly new developments in this rather mature field. Its measurement has proved that a new degree of freedom other than momentum is now available to probe the QGP formation and dynamics. In the hydrodynamic model, unlike particle momentum, polarization is primarily sensitive to the gradients of the hydrothermal fields, and this sensitivity seems to be a unique feature among the known observables. Moreover, polarization can help to constrain the electromagnetic field, which would be incredibly valuable in the search for the chiral magnetic effect (57). The hydrodynamic model predicts, and the measurements have shown, that polarization increases at low energy; this phenomenon will be further explored in future low-energy heavy-ion programs. At RHIC and LHC energies, flow substructure is already being probed in unprecedented detail, presenting theory with new and as yet unsolved challenges. Directions for future studies at these energies have been discussed throughout this review.

There are several pressing issues to be solved that require considerable advances in theory and phenomenology; the most apparent such issue is the discrepancy between the measured and predicted sign of the longitudinal component of polarization as well as the transverse polarization

pattern as a function of the azimuthal angle. Indeed, at this time, after having played the leading role, theory appears to have been surpassed by experiments that have proved able to measure polarization as a function of many relevant variables in relativistic heavy-ion collisions, including azimuthal angle, rapidity, and centrality. In the near future, more measurements [e.g., polarization of different species such as Σ^0 and Ξ^-, spin–spin correlations (104), measurement of polarization in different colliding systems (154)] will be available that will help constrain or disprove theoretical models and assumptions. On the theory side, as has been mentioned, one expects improved formulas including more terms and corrections to Equation 2, the inclusion of dissipative effects, and the application of alternative methods (e.g., kinetic theory) as well as the development of a hydrodynamic with spin potential. Equally important is a major advance in phenomenology and numerical computation that includes hadronic rescattering effects and the systematic study of polarization dependence on the initial conditions.

Since the experimental discovery a few years ago of polarization in heavy-ion collisions, there has been tremendous progress in the study of this phenomenon. Yet, at this early stage, the potential of this new tool is still to be explored. This direction in research may well yield new insights and major results in the study of the QCD matter with nuclear collisions.

DISCLOSURE STATEMENT

ACKNOWLEDGMENTS

LITERATURE CITED

1. Shuryak EV. *Phys. Rep.* 61:71 (1980)
2. Adams J, et al. *Nucl. Phys. A* 757:102 (2005)
3. Adcox K, et al. *Nucl. Phys. A* 757:184 (2005)
4. Back BB, et al. *Nucl. Phys. A* 757:28 (2005)
5. Arsene I, et al. *Nucl. Phys. A* 757:1 (2005)
6. Heinz U, Snellings R. *Annu. Rev. Nucl. Part. Sci.* 63:123 (2013)
7. Adamczyk L, et al. *Nature* 548:62 (2017)
8. Aoki Y, et al. *Nature* 443:675 (2006)
9. Aoki Y, Fodor Z, Katz SD, Szabo KK. *Phys. Lett. B* 643:46 (2006)
10. Becattini F, Fries R. The QCD confinement transition: hadron formation. In *Relativistic Heavy Ion Physics*, ed. R Stock. Landolt-Börnstein—Group I Elementary Particles, Nuclei and Atoms Vol. 23. Berlin: Springer. **https://materials.springer.com/lb/docs/sm_lbs_978-3-642-01539-7_8** (2010)
11. Cooper F, Frye G. *Phys. Rev. D* 10:186 (1974)
12. Becattini F, et al. *Eur. Phys. J. C* 75:406 (2015). Erratum. *Eur. Phys. J. C* 78:354 (2018)
13. Kovtun P, Son DT, Starinets AO. *Phys. Rev. Lett.* 94:111601 (2005)
14. Niemi H, Denicol GS. arXiv:1404.7327 [nucl-th] (2014)
15. Barnett SJ. *Phys. Rev.* 6:239 (1915)
16. Einstein A, de Haas WJ. *K. Ned. Akad. Wet. Proc. Ser. B Phys. Sci.* 18:696 (1915)
17. Tsang MB, et al. *Phys. Rev. Lett.* 57:559 (1986)

18. Lemmon RC, et al. *Phys. Lett. B* 446:197 (1999)
19. Takahashi M, et al. *Nat. Phys.* 12:52 (2016)
20. Saitoh E, Ueda M, Miyajima H. *Appl. Phys. Lett.* 88:182509 (2006)
21. Westfall GD, et al. *Phys. Rev. Lett.* 37:1202 (1976)
22. Poskanzer AM, Voloshin SA. *Phys. Rev. C* 58:1671 (1998)
23. Miller ML, Reygers K, Sanders SJ, Steinberg P. *Annu. Rev. Nucl. Part. Sci.* 57:205 (2007)
24. Liang ZT, Wang XN. *Phys. Rev. Lett.* 94:102301 (2005). Erratum. *Phys. Rev. Lett.* 96:039901 (2006)
25. Gao JH, et al. *Phys. Rev. C* 77:044902 (2008)
26. Abelev BI, et al. *Phys. Rev. C* 76:024915 (2007). Erratum. *Phys. Rev. C* 95:039906 (2017)
27. Becattini F, Piccinini F, et al. *J. Phys. G* 35:054001 (2008)
28. Betz B, Gyulassy M, Torrieri G. *Phys. Rev. C* 76:044901 (2007)
29. Becattini F, Piccinini F. *Ann. Phys.* 323:2452 (2008)
30. Becattini F, Chandra V, Del Zanna L, Grossi E. *Ann. Phys.* 338:32 (2013)
31. Becattini F, Csernai L, Wang DJ. *Phys. Rev. C* 88:034905 (2013). Erratum. *Phys. Rev. C* 93:069901 (2016)
32. Landau LD, Lifshitz EM. *Course of Theoretical Physics*, Vol. 5. Oxford, UK: Butterworth-Heinemann (1980)
33. Becattini F. *Phys. Rev. Lett.* 108:244502 (2012)
34. Becattini F, Grossi E. *Phys. Rev. D* 92:045037 (2015)
35. Becattini F, Cao G, Speranza E. *Eur. Phys. J. C* 79:741 (2019)
36. Tung WK. *Group Theory in Physics*. Singapore: World Scientific (1985)
37. Becattini F, et al. *Phys. Rev. C* 95:054902 (2017)
38. Fang R, Pang L, Wang Q, Wang X. *Phys. Rev. C* 94:024904 (2016)
39. Hattori K, et al. *Phys. Lett. B* 795:100 (2019)
40. Israel W. *Ann. Phys.* 100:310 (1976)
41. Zubarev DN, Prozorkevich AV, Smolyanskii SA. *Theor. Math. Phys.* 40:821 (1979)
42. Bhadury S, et al. arXiv:2002.03937 [hep-ph] (2020)
43. Csernai LP, Magas VK, Wang DJ. *Phys. Rev. C* 87:034906 (2013)
44. Del Zanna L, et al. *Eur. Phys. J. C* 73:2524 (2013)
45. Bozek P, Wyskiel I. *Phys. Rev. C* 81:054902 (2010)
46. Karpenko I, Huovinen P, Bleicher M. *Comput. Phys. Commun.* 185:3016 (2014)
47. Pang LG, Petersen H, Wang XN. *Phys. Rev. C* 97:064918 (2018)
48. Lin ZW, et al. *Phys. Rev. C* 72:064901 (2005)
49. Wheaton S, Cleymans J. *Comput. Phys. Commun.* 180:84 (2009)
50. Karpenko I, Becattini F. *Eur. Phys. J. C* 77:213 (2017)
51. Xia XL, Li H, Huang XG, Huang HZ. *Phys. Rev. C* 100:014913 (2019)
52. Voloshin SA. arXiv:nucl-th/0410089 [nucl-th] (2004)
53. Barros CC Jr., Hama Y. *Int. J. Mod. Phys. E* 17:371 (2008)
54. Barros CC Jr., Hama Y. *Phys. Lett. B* 699:74 (2011)
55. Kapusta JI, Rrapaj E, Rudaz S. *Phys. Rev. C* 101:024907 (2020)
56. De Groot SR, Van Leeuwen WA, Van Weert CG. *Relativistic Kinetic Theory: Principles and Applications*. Amsterdam: North-Holland (1980)
57. Fukushima K, Kharzeev DE, Warringa HJ. *Phys. Rev. D* 78:074033 (2008)
58. Li W, Wang G. *Annu. Rev. Nucl. Part. Sci.* 70:293 (2020)
59. Wang Z, Guo X, Shi S, Zhuang P. *Phys. Rev. D* 100:014015 (2019)
60. Hattori K, Hidaka Y, Yang DL. *Phys. Rev. D* 100:096011 (2019)
61. Gao JH, Liang ZT. *Phys. Rev. D* 100:056021 (2019)
62. Weickgenannt N, et al. *Phys. Rev. D* 100:056018 (2019)
63. Yang DL, Hattori K, Hidaka Y. arXiv:2002.02612 [hep-ph] (2020)
64. Zhang J, Fang R, Wang Q, Wang XN. *Phys. Rev. C* 100:064904 (2019)
65. Li S, Yee HU. *Phys. Rev. D* 100:056022 (2019)
66. Zhang JJ, et al. arXiv:1912.04457 [hep-ph] (2019)
67. Leader E, Lorcé C. *Phys. Rep.* 541:163 (2014)

68. Becattini F, Florkowski W, Speranza E. *Phys. Lett. B* 789:419 (2019)
69. Hehl FW. *Rep. Math. Phys.* 9:55 (1976)
70. Florkowski W, et al. *Phys. Rev. D* 97:116017 (2018)
71. Florkowski W, Ryblewski R, Kumar A. *Prog. Part. Nucl. Phys.* 108:103709 (2019)
72. Florkowski W, Kumar A, Ryblewski R. arXiv:1907.09835 [nucl-th] (2019)
73. Florkowski W, Friman B, Jaiswal A, Speranza E. *Phys. Rev. C* 97:041901 (2018)
74. Florkowski W, Kumar A, Ryblewski R, Singh R. *Phys. Rev. C* 99:044910 (2019)
75. Guo Y, Shi S, Feng S, Liao J. *Phys. Lett. B* 798:134929 (2019)
76. Kharzeev D, Pisarski RD, Tytgat MHG. *Phys. Rev. Lett.* 81:512 (1998)
77. Jinnouchi O, et al. *AIP Conf. Proc.* 675:817 (2003) [*Czech. J. Phys.* 53:B409 (2003)]
78. Anderson M, et al. *Nucl. Instrum. Meth. A* 499:659 (2003)
79. Lee TD, Yang CN. *Phys. Rev.* 108:1645 (1957)
80. Tanabashi M, et al. *Phys. Rev. D* 98:030001 (2018)
81. Adam J, et al. *Phys. Rev. C* 98:014910 (2018)
82. Adam J, et al. *Phys. Rev. Lett.* 123:132301 (2019)
83. Acharya S, et al. *Phys. Rev. C* 101:044611 (2020)
84. Ablikim M, et al. *Nat. Phys.* 15:631 (2019)
85. Zyla P, et al. (Part. Data Group) *Prog. Theor. Exp. Phys.* 2020:083C01 (2020)
86. Braun-Munzinger P, Magestro D, Redlich K, Stachel J. *Phys. Lett. B* 518:41 (2001)
87. Leader E. *Spin in Particle Physics*. Cambridge, UK: Cambridge Univ. Press (2001)
88. Schilling K, Seyboth P, Wolf GE. *Nucl. Phys. B* 15:397 (1970). Erratum. *Nucl. Phys. B* 18:332 (1970)
89. Li H, Pang LG, Wang Q, Xia XL. *Phys. Rev. C* 96:054908 (2017)
90. Vitiuk O, Bravina LV, Zabrodin EE. *Phys. Lett. B* 803:135298 (2020)
91. Sun Y, Ko CM. *Phys. Rev. C* 96:024906 (2017)
92. Ivanov YB, Toneev VD, Soldatov AA. *Phys. Rev. C* 100:014908 (2019)
93. Upsal I. *Global polarization of $\Lambda / \bar{\Lambda}$ in STAR BES*. PhD Diss., Ohio State Univ., Columbus (2018)
94. Lan S, Lin ZW, Shi S, Sun X. *Phys. Lett. B* 780:319 (2018)
95. Adams J, et al. *Nucl. Instrum. Meth. A* 968:163970 (2020)
96. Jiang Y, Lin ZW, Liao J. *Phys. Rev. C* 94:044910 (2016). Erratum. *Phys. Rev. C* 95:049904 (2017)
97. Baznat MI, Gudima KK, Sorin AS, Teryaev OV. *Phys. Rev. C* 93:031902 (2016)
98. Xie Y, Wang D, Csernai LP. *Phys. Rev. C* 95:031901 (2017)
99. Deng WT, Huang XG. *Phys. Rev. C* 93:064907 (2016)
100. Xia XL, Li H, Tang ZB, Wang Q. *Phys. Rev. C* 98:024905 (2018)
101. Wei DX, Deng WT, Huang XG. *Phys. Rev. C* 99:014905 (2019)
102. Wu HZ, Pang LG, Huang XG, Wang Q. *Phys. Rev. Res.* 1:033058 (2019)
103. Csernai LP, Wang DJ, Bleicher M, Stocker H. *Phys. Rev. C* 90:021904 (2014)
104. Pang LG, Petersen H, Wang Q, Wang XN. *Phys. Rev. Lett.* 117:192301 (2016)
105. Adamczyk L, et al. *Phys. Rev. Lett.* 120:062301 (2018)
106. Csernai LP, Strottman DD, Anderlik C. *Phys. Rev. C* 85:054901 (2012)
107. Ivanov YB, Soldatov AA. *Phys. Rev. C* 91:024915 (2015)
108. Bunce G, et al. *Phys. Rev. Lett.* 36:1113 (1976)
109. Heller KJ, et al. *Phys. Rev. Lett.* 41:607 (1978). Erratum. *Phys. Rev. Lett.* 45:1043 (1980)
110. Becattini F, Karpenko I. *Phys. Rev. Lett.* 120:012302 (2018)
111. Niida T. *Nucl. Phys. A* 982:511 (2019)
112. Xie YL, et al. *Phys. Rev. C* 94:054907 (2016)
113. Xie Y, Wang D, Csernai LP. *Eur. Phys. J. C* 80:39 (2020)
114. Magas VK, Csernai LP, Strottman D. *Nucl. Phys. A* 712:167 (2002)
115. Florkowski W, Kumar A, Ryblewski R, Mazeliauskas A. *Phys. Rev. C* 100:054907 (2019)
116. Liu SYF, Sun Y, Ko CM. arXiv:1910.06774 [nucl-th] (2019)
117. McLerran L, Skokov V. *Nucl. Phys. A* 929:184 (2014)
118. Guo X, Liao J, Wang E. *Sci. Rep.* 10:2196 (2020)
119. Skokov V, Illarionov AY, Toneev V. *Int. J. Mod. Phys. A* 24:5925 (2009)

120. Inghirami G, et al. *Eur. Phys. J. C* 76:659 (2016)
121. Inghirami G, et al. *Eur. Phys. J. C* 80:293 (2020)
122. Müller B, Schäfer A. *Phys. Rev. D* 98:071902 (2018)
123. Aggarwal M, et al. arXiv:1007.2613 [nucl-ex] (2010)
124. Han ZZ, Xu J. *Phys. Lett. B* 786:255 (2018)
125. Csernai LP, Kapusta JI, Welle T. *Phys. Rev. C* 99:021901 (2019)
126. Xie Y, Chen G, Csernai LP. arXiv:1912.00209 [hep-ph] (2019)
127. Singha S. arXiv:2002.07427 [nucl-ex] (2020)
128. Kundu S. *Spin alignment measurements of vector mesons with ALICE at the LHC*. Paper presented at Quark
     Matter 2019, Wuhan, China, Nov. 4–9 (2019)
129. Liang ZT, Wang XN. *Phys. Lett. B* 629:20 (2005)
130. Sheng XL, Oliva L, Wang Q. *Phys. Rev. D* 101:096005 (2020)
131. Wang DJ, Néda Z, Csernai LP. *Phys. Rev. C* 87:024908 (2013)
132. Karpenko I, Becattini F. *Nucl. Phys. A* 982:519 (2019)
133. Montenegro D, Torrieri G. *Phys. Rev. D* 100:056011 (2019)
134. Kolomeitsev EE, Toneev VD, Voronyuk V. *Phys. Rev. C* 97:064902 (2018)
135. Deng XG, Huang XG, Ma YG, Zhang S. arXiv:2001.01371 [nucl-th] (2020)
136. Nara Y, Stoecker H. *Phys. Rev. C* 100:054902 (2019)
137. Adamczyk L, et al. *Phys. Rev. Lett.* 112:162301 (2014)
138. Dunlop JC, Lisa MA, Sorensen P. *Phys. Rev. C* 84:044914 (2011)
139. Kekelidze V, et al. *Nucl. Phys. A* 967:884 (2017)
140. Golovatyuk V, et al. *Nucl. Phys. A* 982:963 (2019)
141. Schmidt HR. *J. Phys. Conf. Ser.* 509:012084 (2014)
142. Meehan K. *Nucl. Phys. A* 967:808 (2017)
143. Agakishiev G, et al. *Eur. Phys. J. A* 41:243 (2009)
144. Brodsky SJ, Gunion JF, Kuhn JH. *Phys. Rev. Lett.* 39:1120 (1977)
145. Liang ZT, et al. arXiv:1912.10223 [nucl-th] (2019)
146. Ivanov YB, Soldatov AA. *Phys. Rev. C* 95:054915 (2017)
147. Ivanov YB, Soldatov AA. *Phys. Rev. C* 97:044915 (2018)
148. Alves AA Jr., et al. *J. Instrum.* 3:S08005 (2008)
149. Voloshin SA. arXiv:1710.08934 [nucl-ex] (2017); Voloshin SA. *EPJ Web Conf.* 17:10700 (2018)
150. Majumder A, Van Leeuwen M. *Prog. Part. Nucl. Phys.* 66:41 (2011)
151. Tachibana Y, et al. arXiv:2002.12250 [nucl-th] (2020)
152. Floerchinger S, Wiedemann UA. *J. High Energy Phys.* 1111:100 (2011)
153. Csernai LP, Becattini F, Wang DJ. *J. Phys. Conf. Ser.* 509:012054 (2014)
154. Shi S, Li K, Liao J. *Phys. Lett. B* 788:409 (2019)